nature communications

Article

https://doi.org/10.1038/s41467-025-63716-4

Graphene oxide increases the phototransduction efficiency of copolymeric nanoimplants and rescues visual functions in rat and pig models of *Retinitis pigmentosa*

Received: 7 January 2025

Accepted: 20 August 2025

Published online: 30 September 2025

Check for updates

F. Galluzzi[1,2,9], S. Francia[3,9], S. Cupini[1,4,9], T. Gianiorio[1,4], G. Mantero[1], M. L. DiFrancesco[3], T. Ravasenga[1,3], Jasnoor[1,4], M. Attanasio[5], J. F. Maya-Vetencourt[1,6], G. Pertile[5], D. Ventrella[7], A. Elmi[7,8], M. L. Bacci[7], S. Di Marco[1,3], F. Benfenati[1,4,9] & E. Colombo[1,3,9]

Photoreceptor degeneration in *Retinitis pigmentosa* (RP) is a leading cause of inherited blindness, for which few effective treatments are available. Graphene's exceptional electrical, optical, and mechanical properties, along with its biocompatibility, make it a promising material for retinal stimulation. Building on prior success with conjugated polymers in rodent RP models, we developed injectable retinal nanoimplants that blend a donor-acceptor polymeric architecture with graphene oxide flakes. Here we show that graphene significantly improved the photovoltaic efficiency and enhanced light-evoked responses in blind retinal explants. In RP-affected Royal College of Surgeons rats, a single subretinal injection of these nanoimplants restored light-driven behaviors and visual brain activity at lower luminances than polymer-only particles without any proinflammatory effects. Moreover, this technology restored retinal activity in a pig model of chemically induced degeneration, demonstrating the valuable translational potential of the injectable nanoplatform in the treatment of retinal degenerative diseases.

Degenerative retinal diseases, including *Retinitis pigmentosa* (RP) and age-related macular degeneration (AMD), disrupt the retina's ability to respond to light, ultimately leading to blindness[1,2]. These conditions significantly impact the quality of life of the patients, affecting their financial, social, and mental well-being[3]. RP is a monogenic disorder arising from mutations in genes encoding proteins involved in phototransduction or photoreceptor maintenance and is the most common inherited retinal degeneration[4]. The degeneration typically starts with rods before progressing at varying rates to the cones in the central retina (*fovea centralis*), which are crucial for high-resolution vision and color perception[5]. Although RP is caused by mutations in over 100 distinct genes expressed by photoreceptor cells or the retinal pigment epithelium (RPE), these mutations ultimately lead to photoreceptor cell death through a shared mechanism[6]. On the other hand, the atrophic form of AMD affects 7-8% of the world population and up to 20-25% of the population between 70 and 90 years worldwide and primarily targets foveal cones and perifoveal rods[7–9]. Currently, no effective cure exists for RP or AMD, although gene therapy,

[1]Center for Synaptic Neuroscience and Technology, Istituto Italiano di Tecnologia, Genova, Italy. [2]The Open University Affiliated Research Centre at Istituto Italiano di Tecnologia (ARC@IIT), Genova, Italy. [3]IRCCS Ospedale Policlinico San Martino, Genova, Italy. [4]Department of Experimental Medicine, University of Genova, Genova, Italy. [5]Department of Ophthalmology, IRCCS Sacrocuore Don Calabria Hospital, Negrar, Verona, Italy. [6]Department of Biology, University of Pisa, Pisa, Italy. [7]Department of Veterinary Medical Sciences, University of Bologna, Bologna, Italy. [8]Present address: Department of Veterinary Sciences, University of Pisa, Pisa, Italy. [9]These authors contributed equally: F. Galluzzi, S. Francia, S. Cupini, F. Benfenati, E. Colombo. e-mail: elisabetta.colombo@iit.it

optogenetics, cell therapy, and prosthetic implants have reached the stage of clinical trials with variable results[10–15].

Gene therapy to correct the causative mutation represents the only disease-modifying treatment but faces two major challenges, represented by the large number of genes involved in RP and the need for early intervention when degeneration is at a very initial stage[12]. The other strategies are applicable to all RP mutations and potentially to AMD[16]. Cell therapy with stem cells, photoreceptor precursors, or pigment epithelial cells is emerging as a potentially promising intervention for vision restoration[13,17]. Optogenetics with red-shifted opsins transduced into retinal ganglion cells (RGC) is also providing encouraging results that are temporarily limited by the low light sensitivity of microbial opsins[18]. Sonogenetics has also recently been proposed as a technique to reactivate RGCs transduced with mechanosensitive receptors[19,20]. When photoreceptor degeneration is complete, the most effective strategy is the implantation of a retinal prosthesis that converts the photon energy into an electrical stimulus, activating inner retinal neurons spared by degeneration[11,15].

Retinal prostheses can be made of either inorganic or organic photosensitive materials and can be either planar or a colloidal suspension of nanomaterials. Inorganic planar prostheses have been implanted either epiretinally, directly stimulating RGCs[21], or subretinally, stimulating the second-order neurons and the processing activities of inner retinal networks[22,23]. Among these, the epiretinal Argus II device by Second Sight Medical Products[21] and the subretinal devices Alpha AMS by Retina Implant AG[22] and Prima by Pixium[23] have shown the most promise. In addition to the inherent problems of these devices, such as the need for a power supply, heat production, and scarce biocompatibility, the achieved visual acuity is very low (20/546 for Alpha AMS and 20/460 for Prima). This is the reason why most of these strategies have been discontinued, except for Prima, which is currently under clinical testing in AMD[16]. In addition to silicon-based photodiodes, semiconductive polymers used in organic solar cells have been shown to be effective as an all-organic subretinal planar prosthesis in recovering light sensitivity in preclinical models of RP[24–29]. With respect to inorganic chips, organic semiconductors display good biocompatibility and conformable mechanical properties, although they share with inorganic planar prostheses the same limitations in spatial resolution. All planar prosthetic approaches suffer from the eye curvature that only allows the implantation of small devices, markedly limiting the visual field. Despite this steric limitation, they can be effective in AMD, where the scotoma is limited to the foveal region, or potentially in RP using tiling implants/foldable epiretinal prostheses to cover larger retinal areas[30,31]. In both cases, the current limitation for planar prostheses is the spatial resolution of stimulating units, which are at least 1 to 2 orders of magnitude lower than that allowed by foveal cones, although recent progress has been made in this direction[32].

More recently, colloidal dispersions of poly(3-hexylthiophene-2,5-diyl) (P3HT) nanoparticles were shown to be effective in visual restoration after a minimally invasive subretinal injection in both early- and end-stages of RP, allowing wide retina coverage (>60% of the retina surface) and spatial resolution at the cellular level (nearest-neighbor distance of ≈5 μm)[16,33–35]. Particles are not internalized by neurons or glial cells for up to 8 months in the rat, and remain confined to the subretinal space. In the absence of photoreceptors, they form tight connections with dendrites and cell bodies of bipolar and horizontal cells[33,34]. The mechanism of action of pristine P3HT nanoparticles, clarified by 2D modeling of the neuron-cleft-nanoparticle-extracellular space domain and confirmed experimentally, consists of electrostatic photoactivation of bipolar cells made possible by the pseudo-capacitive charging of the nanoparticle and the highly resistive junctional cleft[34,36].

Starting from the initial formulation of pure P3HT, we sought to improve the phototransduction efficiency of the prosthetic strategy by increasing charge separation and mobility[37] to allow sensitivity to ambient light. On the one side, we considered recreating the bulk heterojunction active in solar cells by blending the p-type conjugated polymer P3HT with n-type organic semiconductors, such as the acceptor phenyl-C61-butyric acid methyl ester (PCBM), already demonstrated to be biocompatible[38]. On the other side, we considered the possibility of creating a hybrid core-shell structure with graphene as an efficient charge extractor[39,40]. Graphene oxide (GO) has long been investigated in organic photovoltaics for its tunable conductive properties and ability to provide a significant decrease of series resistance when used as a charge transport material[41–43]. Various reports have shown how GO is the electron acceptor of choice with respect to pristine graphene or reduced GO when blended with thiophene-based polymers[44–46]. Moreover, its amphiphilic nature also provides easy access to liquid-phase self-assembly approaches, such as reprecipitation and mini-emulsion techniques. Recently, GO nanosheets were also employed as surfactants for the mini-emulsion of P3HT nanoparticles, showing the high potential as an electron extraction material even at the nanoscale[47].

Here, we developed P3HT-based nanoimplants blended with the acceptor PCBM, endowed with a GO core, for exploiting an efficient charge extraction upon illumination when in contact with neurons. The incorporation of GO significantly enhanced the photovoltaic efficiency of the P3HT:PCBM nanoimplants and amplified the light-evoked activity of RGCs in blind retinal explants. Subretinal injection of the GO-cored nanoimplants in the Royal College of Surgeons (RCS) rat model of RP restored light-driven behaviors and visual activities in the absence of pro-inflammatory effects, and with light perception thresholds lower than copolymeric nanoparticles devoid of graphene core Subretinal injection of the GO-cored nanoimplants in the domestic pig, which had undergone toxic photoreceptor degeneration by the administration of iodoacetic acid (IAA), increased the electroretinographic activity, underlining the translational potential of the proposed nanotechnology.

Results

An increased phototransduction efficiency characterizes GO-cored nanoimplants

P3HT: PCBM (PP) and P3HT: PCBM: GO (PPG) nanoimplants were synthesized by the reprecipitation method from tetrahydrofuran (THF) to water under sterile conditions. To verify the stability and reproducibility of the synthesis, we investigated the dimensional and electrical properties of the nanoimplants using dynamic light scattering (DLS; Fig. 1a). Both types of nanoimplants exhibited comparable sizes of ≈180 nm (hydrodynamic diameter), homogeneity (polydispersity index), and colloidal stability (zeta potential). We employed transmission electron microscopy (TEM) to explore the effective entrapment of graphene flakes within the PPGs. The analysis of the sphericity of the nanoimplants revealed that PPGs exhibited a less circular morphology compared to PPs, confirming the encapsulation of sharp geometry GO flakes within the core of the particles (Fig. 1b). We then characterized the photovoltaic properties of the nanoimplants by photo-electrochemical measurements.

To this purpose, we deposited PPGs and PPs onto thin films of indium tin oxide (ITO) on glass substrates by drop-casting and verified their uniform deposition and roughness (rms ~ 50 nm) using atomic force microscopy (AFM; Fig. 1c). We performed cyclic voltammetry recordings in the dark and upon illumination, using the nanoimplant-coated surface as a working electrode (Fig. 1d). The voltammograms obtained from the two types of nanoimplants showed a clear difference in the cathodic evolution of the current density upon green light illumination (540 nm, 25 mW/mm^2), as expected for P3HT-based devices (Fig. 1e)[37,48]. We measured a significant increase in the light-evoked cathodic current density in both groups of samples (Fig. 1f), resulting in a larger light-to-dark ratio for PPGs with respect to PPs

https://doi.org/10.1038/s41467-025-63716-4

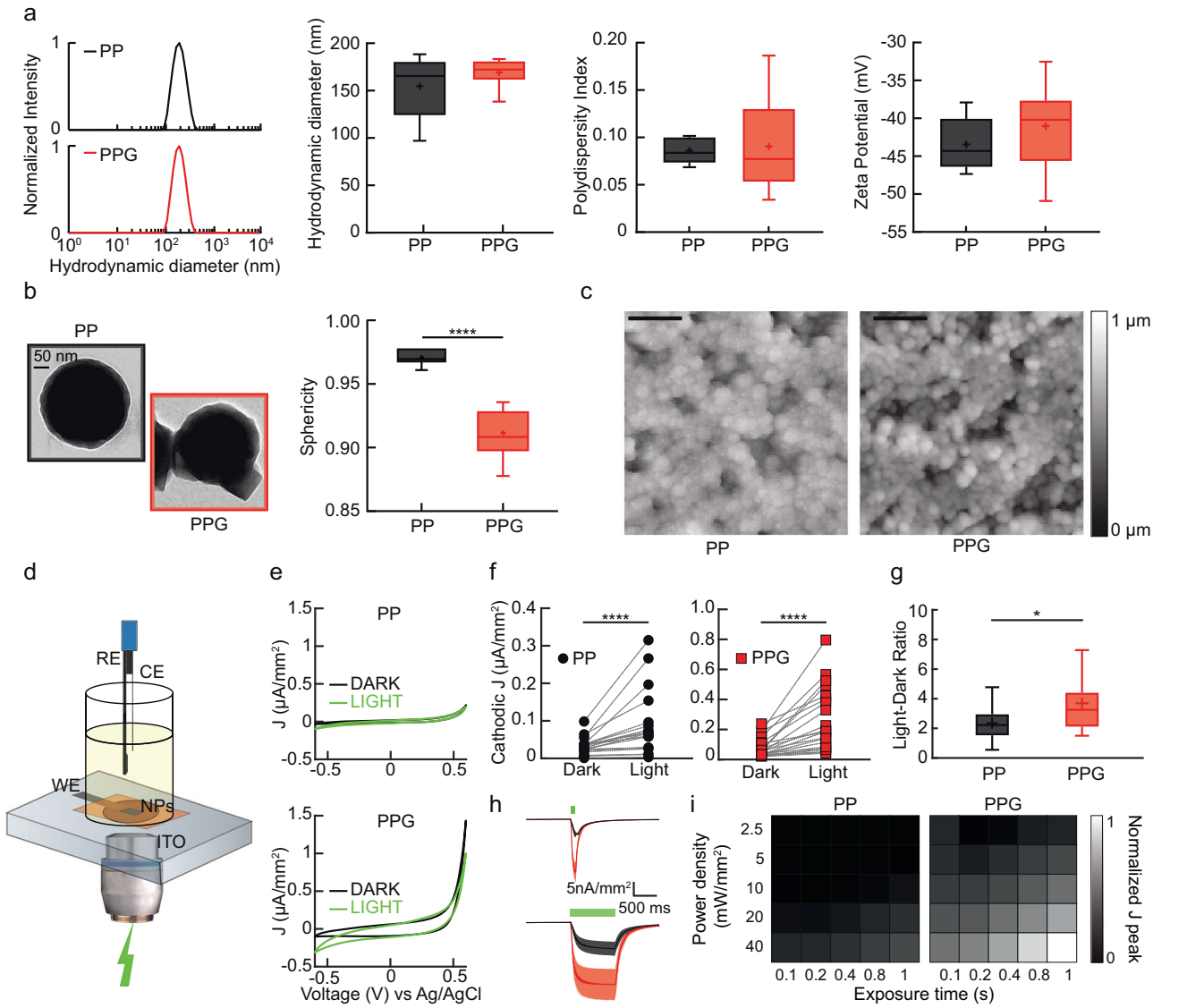

Fig. 1 | Characterization of GO-cored polymeric nanoimplants. a From left to right: DLS characterization of PP (black) and PPG (red) size, hydrodynamic diameter, polydispersity index, and Zeta potential. ($n = 5$ and 9 independent batches of PP and PPG, respectively, from left to right: $p = 0.5158$; 0.5185; 0.4376). **b** Representative TEM image of PPG and PP nanoparticles (NPs) (left) and sphericity index analysis (right) ($n = 7$ for both PP and PPG groups from independent batches, $p < 0.0001$). **c** Representative AFM images of PP (left) and PPG (right) colloidal solutions (20x) deposited onto Indium Tin Oxide (ITO) substrates (scale bar, 1 µm). **d** Schematics of the electrochemical cell for photovoltage and photocurrent measurements of the nanomaterials connected to the working electrode (WE) by silver glue. A sealed electrochemical cell was created above the nanoimplants after applying an insulating tape (Kapton) with a hole to allow the selective exposure of a portion of the droplet. The reference (RE) and the counter (CE) electrodes were dipped in the electrolyte solution (100 mM NaCl) to perform I/V measurements in the dark or upon light excitation (540 nm, 25 mW/mm²). **e** Representative traces of current density (J) vs V for PPs (top) and PPGs (bottom) in the dark (black traces) and upon light excitation (green traces). **f**, **g** Quantification of the photovoltaic effects shows that both PPs and PPGs are active (**f**) ($p < 0.0001$, $n = 20$, 21 nanoimplants depositions for PP and PPG, respectively), but PPGs show significantly larger current increases upon light stimulation (**g**), $p = 0.0229$, $n = 20$, 21 nanoimplants depositions for PP and PPG, respectively). **h** Representative average traces of amperometric measurements (black: PP, red: PPG, bias: −0.6 V) upon green light illumination at two different durations (100 and 1000 ms) at an intensity of 2.5 mW/mm². **i** Heat maps of the normalized current density peaks as a function of stimulus duration (x-axis) and light intensity (y-axis) show a consistently higher photocurrent in PPG (right) compared to PP (left). *$p < 0.05$, ****$p < 0.0001$; Mann-Whitney's U-test (**a**, **g**), two-tailed unpaired Student's t-test (b), Wilcoxon matched-pairs signed rank test (**f**).

(Fig. 1g). Furthermore, we evaluated the temporal dynamics of photocurrent generation using the same setup for both types of nanoimplants through chronoamperometry, by applying a bias potential of −0.6 V and stimulating with light pulses ranging from 100 to 1000 ms. Both nanoimplants showed an immediate response to light illumination for both short and sustained stimulations (Fig. 1h). However, PPG nanoimplants exhibited a consistently higher photocurrent generation across the entire range of stimulation durations, as well as an increased photocurrent generation with rising light intensity (Fig. 1i). This indicates that GO acts as an electric charge transfer booster that, by increasing the light-transduction efficiency of the nanoimplants, can be advantageous for their use as a liquid retina prosthesis.

GO-cored nanoimplants recover light sensitivity in blind retina explants

Once both types of nanoimplants were characterized morphologically and functionally, we investigated whether the higher phototransduction efficiency of PPGs could translate into more sensitive and effective modulation of neuronal activity. We first tested the colloidal stability of the nanoimplants in culture medium (Supplementary Fig. 1). Both

PPs and PPGs displayed a high stability in both water and culture medium, with constant hydrodynamic diameter over time. Next, we tested the biocompatibility of the nanomaterials incubated with primary neuronal cultures up to 6 days in vitro and analyzed them by confocal microscopy. By exploiting the intrinsic fluorescence of P3HT, we confirmed that both PPs and PPGs decorate the surface of neuronal membranes, covering ~0.5% of the neuronal plasma membrane, without a significant internalization over the tested time points (Supplementary Fig. 2a, b)[33,36]. Patch-clamp recordings demonstrated that green light pulses effectively modulate membrane potential and the firing activity of neurons treated with either PPs or PPGs, as compared to inert silica particles of the same diameter (SiO_2; Supplementary Fig. 2c, d). In line with previous in vitro electrophysiological results with graphene-based photosensitive planar interfaces, nanoimplants triggered hyperpolarization of the neurons during illumination, potentially rendering neurons more excitable by an anode break mechanism[27,49].

Next, we focused our attention on the stimulation of explanted retinas from >10-month-old dystrophic RCS rats bearing a loss-of-function mutation in the *Mertk* gene[50]. At this age, photoreceptors are absent, and the inner retina is markedly rewired[34,51,52]. Retinas were dissected along with the choroid/sclera, cut into small patches, and acutely injected with the colloidal solutions in the subretinal space, mimicking the in vivo subretinal injection of the nanoimplants. The retinal preparations were placed RGC-down onto multielectrode arrays (MEAs), and the firing activity of RGCs was recorded under basal conditions and in response to light stimulation (Fig. 2a).

The peristimulus time histogram (PSTH) of the single unit firing activity of RGCs upon 200-ms pulses of green light showed no relevant effects for retinas treated with SiO_2, except for a slow and modest light-dependent response to the longer light stimulus (200 ms) that is likely attributed to a thermally induced increase of the basal spontaneous firing. Under the same stimulation conditions, both PPs and PPGs gave rise to an overall increase in the firing frequency that was time-locked with the light stimulus and enhanced when PPGs were used (Fig. 2b). The blind retinal explants injected with the nanoimplants were subjected to 540-nm 10-mW/mm^2 light stimuli of various durations (10 or 200 ms) administered at 0.25 Hz. The retinas treated with the PPG formulation displayed a significantly higher percentage of electrodes with light-dependent firing modulation in response to both 10-ms and 200-ms stimuli with respect to retinas treated with control SiO_2, while PPs only responded to the 200-ms stimuli (Fig. 2c). Analysis of the firing activity revealed that GO-cored nanoimplants elicited a significant RGC firing with respect to retinas treated with SiO_2, even with the shorter pulses (10 ms), while the firing response of PPs under these conditions was not different from the control. When longer (200 ms) pulses were used, the light-evoked neuromodulation by PPs became significant. However, also under this condition, PPGs outperformed

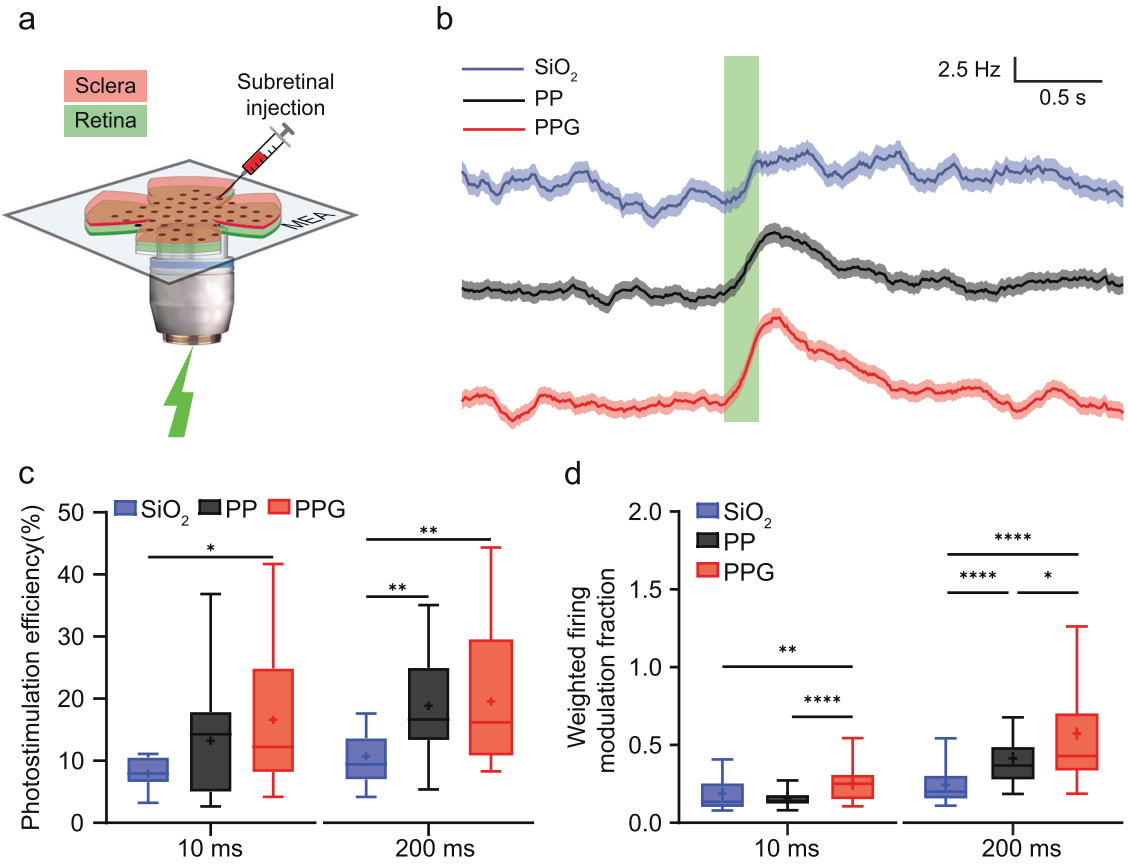

Fig. 2 | Nanoimplants photostimulate RGCs in blind retinal explants. **a** Schematic representation of acute subretinal particle injections in retinal explants from RCS rats. RGC activity in the dark and upon green light stimulation (green arrows, 540 nm, 10 mW/mm^2) was recorded with multielectrode arrays (MEAs). **b** Representative peristimulus time histograms (PSTHs) of single unit RGC firing rates (bin, 10 ms; mean ± SEM) in retinal explants injected with either SiO_2 used as a control (blue), PPs (black), or PPGs (red) upon green light stimulation (green bar; 25 sweeps, 200 ms light ON, 10 mW/mm^2). **c** Photostimulation efficiency for the various materials was calculated as the ratio between the number of photoactivated units and the total number of recorded units for each retinal explant (10 ms: $n = 14$, 17, 20 retinal explants; 200 ms: $n = 18$, 24, 31 retinal explants. 10 ms: SiO_2 vs PPG $p = 0.0435$; 200 ms: PP vs SiO_2 $p = 0.0012$, PPG vs SiO_2 $p = 0.0010$). **d** Firing rate modulation (baseline vs 200–700 ms after light onset and weighted by the photostimulation efficiency) induced by the nanoimplants under various light stimulation conditions ($n = 13$, 24, and 34 neurons at 10 ms/10 mW/mm^2; $n = 14$, 22, and 25 at 200 ms/10 mW/mm^2; for SiO_2, PPs, and PPGs, respectively, from > 8 RCS rats. 10 ms: SiO_2 vs PPG: $p = 0.0045$; 200 ms PP vs PPG: $p = 0.0268$). $^*p < 0.05$, $^{**}p < 0.01$, $^{****}p < 0.0001$; Kruskal-Wallis ANOVA/Dunn's tests.

PPs with a light-dependent increase in RGC firing that was significantly more intense (Fig. 2d). The presence of a significant firing stimulation by PPGs at the lower pulse duration testifies to the enhanced phototransduction efficiency attributable to the core-shell interface and demonstrates the potential of the graphene-based engineering of the nanoimplants.

Subretinal injection of the GO-cored nanoimplants in dystrophic RCS rats does not induce retina inflammation

We next tested the in vivo efficacy in visual restoration of the superior performance of PPGs. We subretinally injected 3/4-month-old pink-eyed albino RCS rats with either PPG or SiO_2 (sham) suspensions and compared their visual performances with those of untreated RCS rats and congenic healthy RDY rats between 1 and 4 months after surgery (Supplementary Fig. 3). At the age of surgery, retinal degeneration in this strain of rats is almost terminal, and light perception is completely lost before 3 months of age[34,53].

We first verified the distribution of PPGs in whole-mount retinas analyzed by transmission microscopy, thanks to the strong absorption of P3HT in the visible range (Fig. 3a) and by confocal fluorescence microscopy of the intrinsic fluorescence of polythiophene (Fig. 3b). We first generated masks in tile-scan mosaics and then calculated the total area of PPGs and the percent of retinal coverage. The analysis revealed a widespread distribution of PPGs in the subretinal space with a total area of 0.33 ± 0.08 mm^2 (mean ± SEM) with a retinal surface coverage of 56 ± 3 % (mean ± SEM) in the absence of overt aggregation (Fig. 3c). The regional distribution of PPGs was also addressed by aligning the retinas based on the injection petal and then subdividing the retinal surface into radial/concentric sectors to calculate the number and density of the nanoimplants (see "Methods"). The results of this analysis show that, although the highest density values are reached in the proximity of the injected sector, a significant spread of PPGs to large distances within the subretinal space was observed, covering a wide fraction of the retinal surface (Fig. 3d).

We previously showed that pristine P3HT nanoparticles are fully biocompatible, and their subretinal implantation does not elicit any retina inflammation or gliosis. However, since PPGs contain the acceptor PCBM and the GO core, we explanted the injected retinas from the animals of the four experimental groups (RDY, RCS, RCS +SiO_2, RCS + PPG) and performed immunohistochemical analysis. Retinas were first studied by using the Hoechst nuclear staining to identify retinal layers and verify the cellularity of the outer nuclear layer (ONL), containing photoreceptor cell bodies. The photoreceptor nuclei, densely packed in the ONL of healthy RDY retinas, were completely absent in all

RCS groups, irrespective of whether they were non-injected, injected with PPGs, or sham-injected with SiO_2, ruling out any trophic effect induced by the surgical procedure or the presence of nanoimplants (Fig. 3e, f).

We then performed immunohistochemistry to investigate the expression of markers of microglia (ionized calcium-binding adapter molecule 1, Iba-1; Fig. 3e) and Müller cells/astrocytes (glial fibrillary acidic protein, GFAP; Fig. 3f) to ascertain the presence of possible proinflammatory effects of the injected materials. Dystrophic RCS rats injected with either SiO_2 or PPGs displayed levels of microgliosis comparable to those observed in untreated RCS rats, suggesting that the surgical procedure per se and the prolonged presence of the materials in the subretinal space did not exert proinflammatory effects (Fig. 3g). Since a less ramified/ameboid-like morphology characterizes the activated microglia, Iba-1-positive cells were also monitored by Sholl analysis for the number of ramifications. No significant differences in the number of intersections were observed across the four experimental groups, indicating no signs of microglia activation (Fig. 3h). Although phagocytosis of PPG by Iba1-positive cells was rarely observed, we double-checked the presence of an inflammatory response by double-staining Iba1-positive microglial cells with CD68, a marker of microglia phagocytic activation. We found that the subretinal injection of PPGs did not lead to an increased CD68-positive cell fraction, indicating the absence of microglial activation in the ONL as well as in the total retina (Supplementary Fig. 4). When GFAP immunoreactivity in the ONL was analyzed, the degree of astrogliosis was comparable between untreated and injected dystrophic RCS rats, while it was nearly undetectable in healthy RDY rats (Fig. 3i). Taken together, the data suggest that the activation of microglia and macroglia observed in the RCS rat retina is independent of surgery and the implanted material and only attributable to the ongoing degeneration of the outer retina.

GO-cored nanoimplants restore light-driven behavioral responses in blind RCS rats

We next investigated whether PPGs could improve the restoration of visual percepts in dystrophic RCS rats (see the timeline of experiments in Supplementary Fig. 3). One month before the subretinal injection (MBI), the animals were subjected to the light-dark box test, which, by leveraging the innate aversion of rats to illuminated areas and resulting anxiety, enables the evaluation of light-sensitivity (Fig. 4a)[54]. One month after injection (MPI), the latency of escape from the illuminated compartment was significantly shortened in PPG-injected animals and fully recovered to the levels of untreated RDY controls (Fig. 4b). Moreover, the analysis of the time spent in the two compartments revealed that PPG-injected animals recovered the preference for the dark compartment typical of normally sighted RDY controls, while SiO_2-injected RCS rats did not differ from untreated blind animals (Fig. 4c). The analysis of the number of transitions between the two compartments, a proxy of potential motor impairments that could have biased the results, revealed no differences across the four experimental groups (Supplementary Fig. 5a). When a direct comparison in the light preference of PP- and PPG-injected animals was performed and compared with non-injected RCS rats and RDY controls, PPG-injected animals exhibited a dark preference fully overlapping that of healthy RDY rats, which was slightly better than that obtained with PP injection (Supplementary Fig. 6).

To further prove the recovery of visual information processing at the cortical level, animals were subjected to classical Pavlovian conditioning, using a mild electric foot shock as the unconditioned stimulus (US) and light flashes as the conditioned stimulus (CS). Light-shock pairing involves high-order brain areas, including projections from the lateral geniculate nucleus to the V1/V2 cortex, visual association area TE2, perirhinal cortex, and the amygdala[55,56]. During the conditioning session, animals were dark-adapted for 2 min and then exposed to a CS-US pairing. Once trained (conditioned), they were placed in a different environment and cued with the CS after 2-min dark adaptation to assess their light-related freezing response based on the recall of implicit memory formed during the training phase. Finally, to verify the absence of contextual conditioning, animals were placed again in the conditioning environment and exposed to the dark for 5 min without US presentation (context session; Fig. 4d). The fear reaction to the light stimulus during the training phase was similar across the four experimental groups that exhibited a progressively increasing freezing response to CS + US pairing (Fig. 4e). In the cue session, PPG-injected RCS rats demonstrated a significant increase in light-conditioned freezing behavior that was indistinguishable from the behavioral response of healthy RDY controls. In contrast, untreated and SiO_2-injected RCS rats did not show any increase in the freezing response (Fig. 4f). When the frequency of the freezing events was analyzed as a function of time, both PPG-injected RCS rats and healthy RDY rats showed a similar increase in the frequency of freezing events starting at the onset of light stimulation and lasting for over 2 min (Fig. 4g), while the freezing responses were negligible in both sham- and non-injected RCS rats (Fig. 4h). When the animals were

https://doi.org/10.1038/s41467-025-63716-4

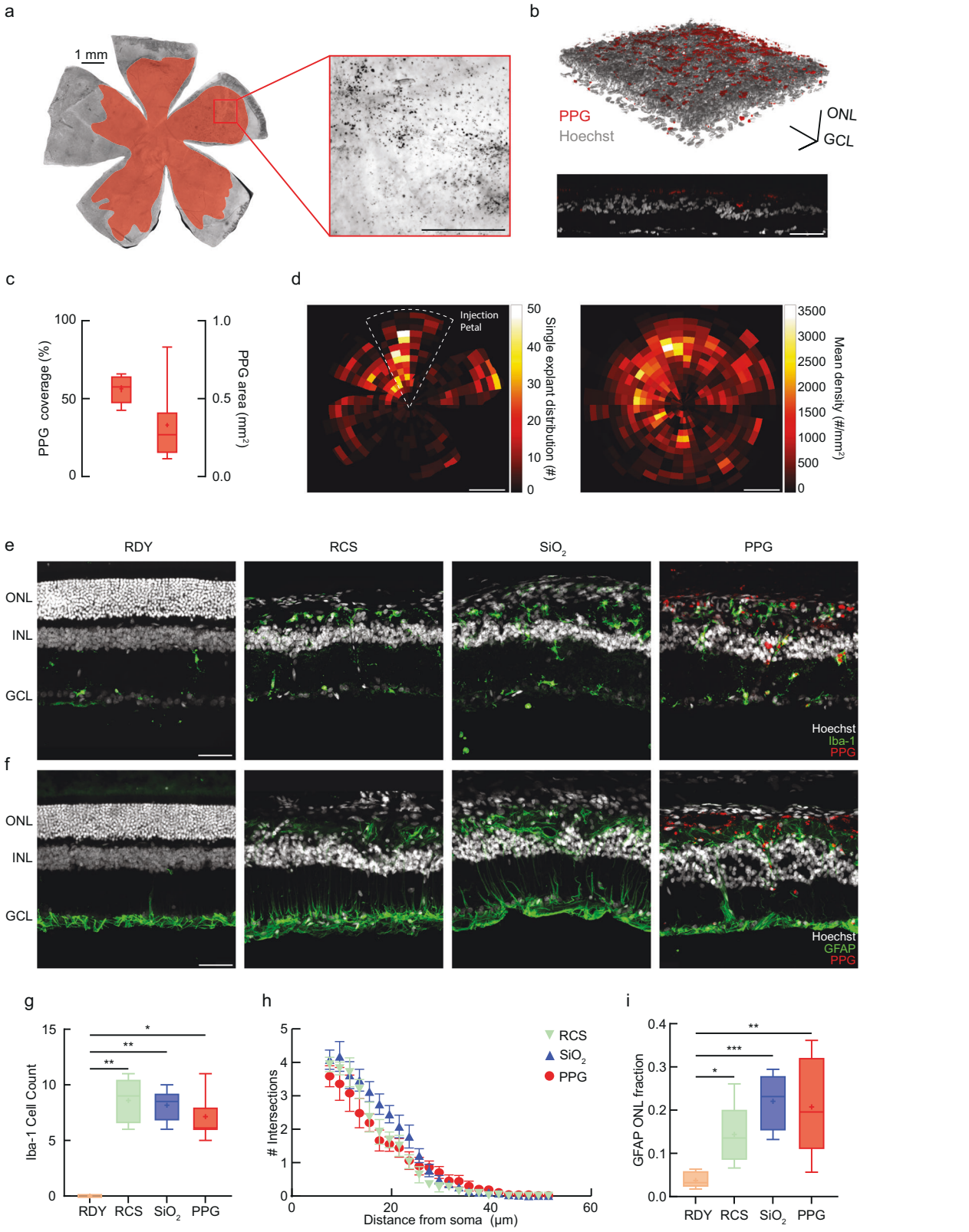

subjected to the control context test, using the same environment experienced in the conditioning phase, the recorded freezing behavior did not differ across the experimental groups (Supplementary Fig. 5b).

To address whether PPGs outperform PPs, we developed an experimental protocol for light-cued conditioning specifically designed to assess perceptual thresholds. While conditioning was still performed at 22 Lux, in the cue phase, increasing light intensity stimuli (2.5-22 Lux) were tested to evaluate the threshold for the conditioned response (Fig. 4i). The results show that normally sighted animals have a very low perceptual threshold to evoke the conditioned freezing response (2.5 Lux; Fig. 4j), which is fully matched by RCS rats injected with PPGs. In contrast, animals injected with PP nanoimplants show a higher threshold (5 Lux), while blind animals cannot be conditioned at any light intensity (Fig. 4j, k).

Fig. 3 | Retinal distribution and biocompatibility of subretinal nanoimplants in the RCS rat. a Left: Representative image of an in vivo PPG-injected whole-mount RCS rat retina (scale bar, 1 mm). The red area represents the retina surface where PPGs are located. Right: At higher magnification, PPGs appear as dark dots in brightfield transmitted light (scale bar, 0.5 mm). **b** Top: 3D reconstruction of a retinal field with super-resolution confocal microscopy showing the localization of intrinsically fluorescent PPGs (red) at the level of the ONL (scale bar, 50 μm); bottom: single zx transversal section of the 3D reconstruction showing the presence of PPG only in the ONL. **c** Tukey-style box plots of the percentage of retina surface covered by PPGs and their total sectional area ($n = 8$ whole-mount retinal explants from $n = 8$ animals). **d** Left: Representative heatmap distribution of the PPG numbers across a single whole retina explant. The white dashed contour indicates the petal of the injection site. Right: Heatmap of the mean PPG distribution density calculated across all retinal explants, following the alignment of each explant to the injection site petal (scale bar, 2 mm). **e**, **f** Representative images of retinal cross-sections from the 4 experimental groups that were double-labeled for either Iba-1 positive microglial cells (**e**; green) or the Müller cell/astrocyte marker GFAP (**f**; green), merged with nuclear staining with Hoechst (white) and P3HT intrinsic fluorescence (red, scale bar, 50 μm). Abbreviations: ONL, outer nuclear layer; INL, inner nuclear layer; GCL, ganglion cell layer. Scale bars, 50 μm. **g**, **h** Quantification of Iba-1-positive cells counted at the ONL level (**g**) and respective Sholl analysis showing branch extensions from the cell soma (h, mean ± SEM) ($n = 7,5,6,7$ animals for RDY, RCS, SiO_2, and PPG, respectively, g: RDY vs RCS, SiO_2, PPG: $p = 0.0037$, 0.0048, 0.0496). **i** Quantitative analysis of GFAP expression, calculated as the ratio between the immunoreactivity density in the ONL and the total integrated retinal density (ONL + IPL + GCL) ($n = 7,8,6,6$ for RDY, RCS, SiO_2, and PPG, respectively). $^*p < 0.05$, $^{**}p < 0.01$, $^{***}p < 0.001$; Kruskal-Wallis/Dunn's test (g), two-way ANOVA/Tukey's test (h), ordinary one-way ANOVA Tukey's test (i).

GO-cored nanoimplants restore subcortical and cortical responses to light and recover visual acuity in blind RCS rats

To analyze the restoration of light sensitivity at the subcortical level, we measured the pupillary light reflex (PLR) that, triggered by the complementary action of photoreceptors and intrinsically photosensitive RGCs (ipRGCs), operates through bilateral retinal connections to the pretectal area of the brainstem. One eye of the animals was placed in front of a stimulating green LED (530 nm at 5–50 lux), and the contralateral eye was illuminated with infrared light (780 nm) and placed in front of a recording camera (Fig. 5a)[34]. RCS rats implanted with PPGs, regardless of the light intensity, showed an extent of pupil constriction that was indistinguishable from that obtained from healthy RDY controls and significantly higher than that of either untreated or SiO_2-injected RCS rats (Fig. 5b). To assess the better performance of PPGs over PPs and evaluate the PLR threshold, we evoked the PLR at increasing light intensities from 1 to 5 Lux. RCS rats implanted with PPGs rescued the PLR at 2 Lux, while blind animals injected with PPs displayed a significant pupil constriction only at 5 Lux (Supplementary Fig. 7).

We next examined light sensitivity and visual acuity at the cortical level by recording visually evoked potentials (VEPs) in the binocular region of the primary visual cortex (V1, OC1b) in response to patterned stimuli (Fig. 5c)[34]. Anesthetized rats were cued with a random sequence of contrast reverse square wave gratings (1 Hz) at increasing spatial frequencies (0.017-1 cycles/degree, CPD). RCS rats injected with PPGs showed a significantly higher percentage of responses compared to the two blind control groups (Fig. 5d, e), as well as a much higher VEP amplitude at the lowest spatial frequencies tested (0.017 and 0.032 CPD; Fig. 5f). Although PPG-implanted RCS rats could not completely recover the VEP amplitude expressed by healthy RDY rats, they could reach ≈ 86 % of the visual acuity of healthy RDY rats, proving the effective restoration of spatially resolved vision (Fig. 5g).

Translation of GO-cored nanoimplants in the domestic pig

As a step towards the translation of subretinal nanoimplants to clinical applications, we subretinally injected PPGs in the domestic pig, an excellent animal paradigm to test therapeutic strategies for photoreceptor degeneration[28,57,58]. In particular, the pig's eye size and vascularization are very similar to the human eye and allow for the precise setup of the surgical procedure (Fig. 6a). To induce photoreceptor degeneration, four 12-month-old wild-type domestic pigs were administered a calibrated dose of the glycolysis inhibitor IAA in the ear vein following (see protocol in Supplementary Fig. 8), as previously described by us and others[59–63]. At the same time, two animals received only saline and were used as healthy controls. IAA effectively disrupted retinal integrity with a widespread degeneration of rods and cones (Fig. 6b) that rendered the retina of the lesioned pigs bilaterally insensitive to light. Electroretinogram (ERG) recordings in response to either scotopic or photopic stimuli, performed two weeks after the IAA injection, highlighted the disappearance of the a-wave, physiologically attributable to photoreceptor activation, and a strongly compromised b-wave generated by the activity of 2nd order neurons (Fig. 6c, d). In parallel, in vivo optical coherence tomography (OCT) analysis showed the disruption and thinning of the outer retina in the IAA-injected pigs with respect to saline-injected healthy controls (Fig. 6e).

Both control and IAA-treated animals were subretinally injected with PPGs in the left eye and inert SiO_2 in the right eye. The subretinal surgery did not trigger retinal detachment regardless of the type of injected materials, as shown by the representative OCT images of Fig. 6e. PPGs were well-distributed throughout the retina, predominantly concentrated in the residual ONL, as illustrated by the representative maximum projection and reconstruction of a retina injected with PPGs (Fig. 6f). The rescue of light-evoked retinal activity was evaluated by ERG recordings performed at scotopic and photopic luminance levels on both eyes of anesthetized animals. In healthy control pigs, due to the long-lasting inflammatory response caused by subretinal injection surgery[64,65], the post-surgery ERGs exhibited a reduced amplitude of both a- and b-waves with respect to the ERG recorded before the surgery (Supplementary Fig. 9). However, the amplitude of the b-waves of the eyes injected with PPGs was not significantly different from those generated by SiO_2-injected eyes. In contrast, in pigs with IAA-induced retinal damage, the eyes injected with PPGs recovered their b-wave signature significantly better than the ones injected with inert SiO_2 (Fig. 6g). The data obtained in the pig demonstrate the potential of the GO-cored nanoimplants as a prosthetic strategy for human RP.

Discussion

The generation of retinal prostheses to reactivate the light-dependent activity of the inner retina and emulate natural vision in retinal dystrophies is in great demand. The last two decades have witnessed an intense development of silicon- and polymer-based planar photovoltaic prostheses that can replace the lost photoreceptors and stimulate the inner retinal circuits in a light-dependent fashion[10,15]. However, these strategies have specific drawbacks. Planar devices must be small to comply with the eye curvature, implying a minimal visual field (the so-called "tunnel vision"), and require troublesome implantation surgery. While the narrow visual field may not be a problem to correct AMD, and the possibility of using tiling implants or foldable epiretinal devices may extend the field of view, the main problem remains the limited spatial resolution of the stimulating units, that despite recent advances in nanofabrication, remains at least one order of magnitude lower that that allowed by foveal cones[30–32].

To overcome these limitations, various types of nanoparticles (NPs) have been explored for neuronal photostimulation and the treatment of degenerative blindness. Rare earth or platinum NPs have shown promise in mitigating photoreceptor degeneration caused by excessive free radical production[66,67]. Neuron-targeted gold NPs can

https://doi.org/10.1038/s41467-025-63716-4

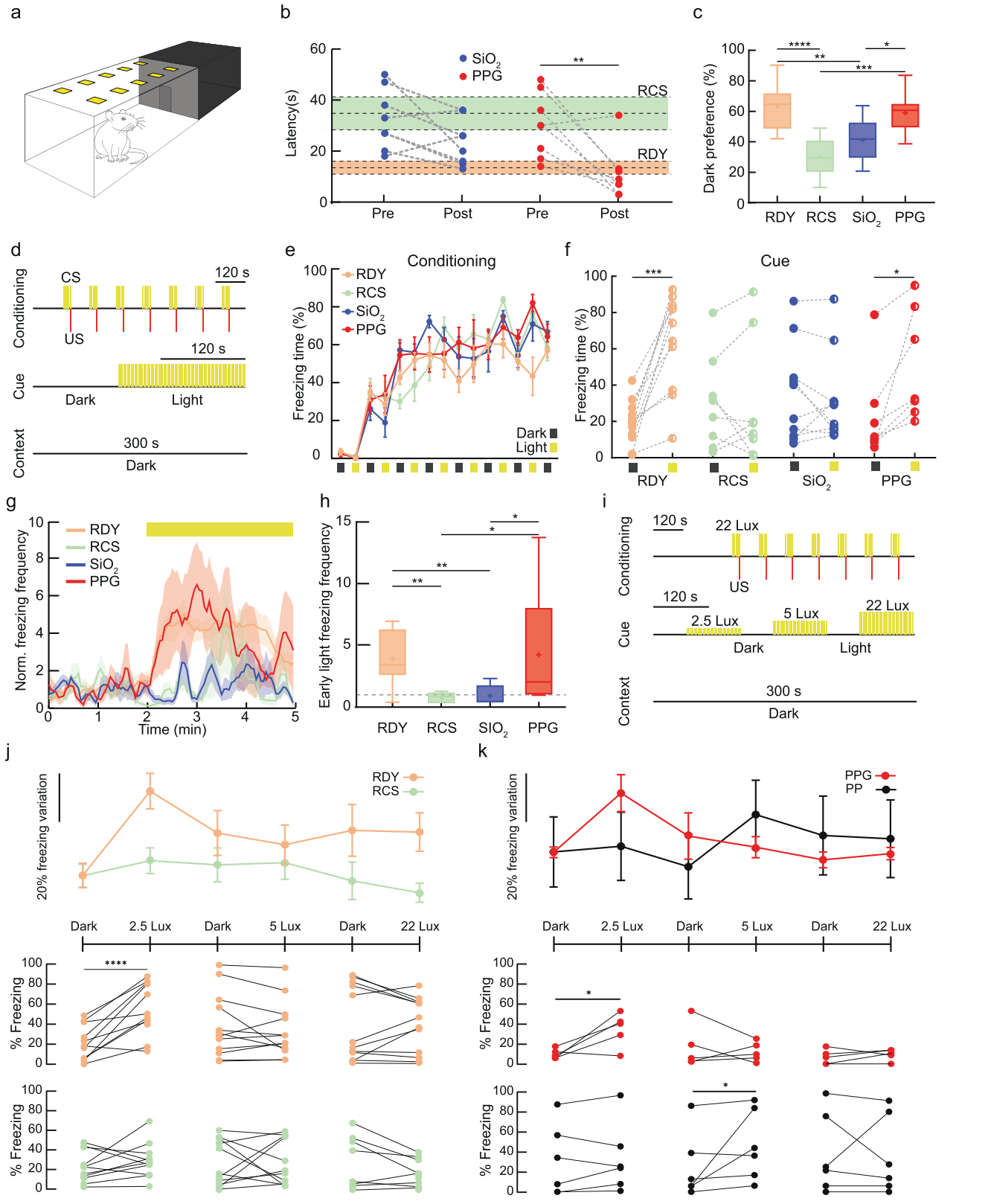

facilitate photothermal neuronal stimulation[68–71]. Additionally, infrared-sensitive upconverting NPs can activate optogenetic actuators[72] or endogenous photoreceptors[73], effectively granting sensitivity to infrared light. Conversely, semiconducting NPs, whether organic or inorganic, excel in generating long-lived interfacial charges, enabling functionalities such as current generation, faradaic reactions, or electrostatic effects[16]. NPs have many advantages over planar prostheses, as they are minimally invasive, cover a large part of the retina surface, and act at the single-cell level with a high potential for spatial resolution[16]. Recently, we pioneered mono-component polythiophene semiconducting NPs for neuronal stimulation and visual restoration in both the early and end stages of RP[33,34]. However, one of the significant problems of mono-component P3HT NPs is the poor light-transduction efficiency due to the relatively low charge

Fig. 4 | The subretinal nanoimplants in RCS rats restore light-driven behaviors. **a** Schematic of the light-dark box test to assess light-driven behavior. **b** Light-to-dark escape latency for animals before and after injection ($n = 14$, 11, 8, and 8 animals for RDY, RCS, SiO_2, and PPG, respectively, $p = 0.0073$). **c** Box plots of the dark preference over the total time of the test ($n = 14$, 9, 8, and 11 animals for RDY, RCS, SiO_2, and PPG, respectively, RDY vs SiO_2, RCS: $p = 0.0048$, <0.0001; PPG vs SiO_2, RCS: $p = 0.0410$, 0.0002). **d** Diagram of the conditioning protocol (conditioned stimuli, CS; light flashes at 5 Hz; unconditioned stimuli, US). **e** Conditioning session ($n = 11$, 8, 10, and 7 for RDY, RCS, SiO_2, and PPG, respectively, mean ± SEM). **f** During the cue test session, increased light-conditioned freezing behavior was observed in both RDY and PPG ($n = 14$, 9, 8, and 11 for RDY, RCS, SiO_2, and PPG, respectively; RDY: $p = 0.0001$, PPG: $p = 0.0156$). **g** Time course of the frequency of freezing events (bin, 3 s) normalized for the baseline freezing behavior in the dark. Shaded areas indicate ± SEM. **h** Freezing frequency during the first minute of illumination. The dashed line represents the average baseline frequency of freezing events ($n = 10$, 8, 8, and 7 animals for RDY, RCS, SiO_2, and PPG, respectively; RDY vs RCS, SiO_2, and PPG: $p = 0.0024$, 0.0018, and 0.4590, respectively; RCS vs PPG: $p = 0.0380$; SiO_2 vs PPG: $p = 0.0306$). **i** Experimental protocol for light-cued conditioning to identify the visual perception threshold with cues at 2.5, 5, and 22 Lux. **j** Percentage change in cue freezing behavior ($n = 12$ and 11 animals for RDY and RCS, respectively). Top: Dose-response freezing variation (mean ± SEM). Bottom: Difference in freezing between dark and light conditions. RDY rats have a threshold at 2.5 Lux ($p < 0.0001$). **k** Freezing behavior of PPG or PP shown as in panel j. PPG shows a perceptual threshold at 2.5 Lux ($p = 0.0218$), while PP exhibits a freezing peak at 5 Lux ($p = 0.0312$) ($n = 5$ and 6 animals for PP and PPG, respectively). $^{*}p < 0.05$, $^{**}p < 0.01$, $^{***}p < 0.001$, $^{****}p < 0.0001$; two-tailed paired Student's t-test (**b**); one-way ANOVA/Tukey's test (c); two-tailed paired Student's t-test/Wilcoxon matched-pairs signed rank test (f, j, k); Kruskal-Wallis ANOVA/Dunn's tests (**h**).

separation and mobility that trigger the formation of the nano-dipole, modulating the electrical state of the neuronal membrane.

In this paper, we introduced an innovative nanoarchitecture to boost phototransduction efficiency, which can translate into a more efficient visual restoration with improved sensitivity to the low luminances typical of scotopic vision. We first reproduced the bulk heterojunction of solar cells by blending P3HT with an efficient acceptor such as PCBM. Then, we created core-shell structures by coating a core of GO with the polymeric blend. In the last few years, graphene has attracted great interest for its biomedical applications due to its mechanical properties, flexibility, transparency, thermo-electrical conductivity, and excellent biocompatibility with neural tissues[39,40,74,75]. Indeed, core-shell PPGs outperformed heterojunction PPs, consistent with the excellent charge extraction properties of GO, resulting in an enhancement of the photocurrents and efficiency of the optoelectronic devices. These findings were mirrored by a significantly higher light-dependent stimulation RGC firing activity in blind retinal explants, also at power densities and light stimulus duration conditions under which P3HT NPs and heterojunction PPs were not effective, testifying to the potential of core-shell PPGs for in vivo studies. Although the power intensities employed to stimulate retinal explants are considerably higher than those of the in vivo experiments, they are in the same range as those used under ex vivo conditions for photoactive interfaces or optogenetics[16]. Moreover, the significant firing response of RGCs in PPGs injected blind retinas to 10-ms stimuli rules out the possibility of a thermal effect due to the absorbance of P3HT, demonstrating the potential of the graphene-based engineering of the nanoimplants.

Subretinally injected PPGs in RCS rats displayed a wide distribution in all retinal sectors 3-4 months after subretinal injection, ensuring an extended visual field. Except for occasional findings of nanoimplants reaching the inner retina or being internalized by microglia or RPE, the vast majority of PPGs stably populated the subretinal space without being cleared over time. This observation fully agrees with the data obtained with pristine P3HT NPs, which were found to cover over 60% of the retinal surface and to remain constrained in the subretinal space for up to 8 months after subretinal administration[33,34]. Due to the overlapping location, the cellular targets of PPG photostimulation will be the same as shown by Francia et al. (2022)[34], i.e., the dendritic arbor and the cell bodies of bipolar and horizontal cells physiologically synapting in the outer plexiform layer (OPL). It is known that dendrites of bipolar cells abnormally proliferate during degeneration and extend towards the subretinal space[76–78], enabling stimulation of dendritic ramifications by the nanoimplants. Although ex vivo evidence has shown that RGCs can be activated with direct puffs of pristine P3HT NPs onto the cell body at high stimulation powers[33], RGCs are not likely the targets of photostimulation by the nanoimplants in vivo, because of the only occasional presence of PPGs in the GCL and the large size and high threshold for action potential firing of RGCs.

Because of their carbon-based nature resembling endogenous macromolecules, PPGs did not trigger retina stress or significant inflammatory reactions. No astrogliosis or microgliosis was observed after PPG injection. Despite sporadic findings of a PPG internalized by a microglial cell, microglia displayed a physiological ramification of cell processes and normal expression of CD68, testifying to the absence of phagocytosis and microglia activation induced by PPGs. Although for any subretinal intervention, there is the possibility of damaging the retina, for colloidal suspensions of organic NPs, this risk is minimized by the low invasiveness of the microinjection. Consistent with their increased phototransduction efficiency, PPGs effectively rescued visual activity in dystrophic rats. Most of the subcortical and cortical visual responses, such as the PLR, light-driven behavior, visual acuity, and the formation/recall of light-cued implicit memories, were restored to the levels of age-matched healthy rats with the same genetic background. This demonstrates that not only do PPGs operate a light-dependent activation of the inner retina, but that this effect triggers a full reactivation of the visual system up to visual perception in the primary visual cortex and high-order multisensory areas. The increased transduction efficiency due to the graphene core in PPGs translated into a lower intensity threshold to evoke behavioral responses to light stimuli that was apparent both in the PLR (2 *vs.* 5 Lux of PPs) and in the freezing responses in light-cued classical conditioning paradigms (2.5 vs. 5 Lux of PPs), fully confirming in vivo the results of the in vitro and ex vivo studies. Moreover, the maximum luminance employed in our in vivo studies is two orders of magnitude lower than the permissible safety conditions for ocular safety[16].

In view of a translation of our findings to the human disease, we implanted PPGs in the retina of domestic pigs. The pig is an excellent preclinical model for therapeutic ophthalmological strategies[28,57,58]. Although mutant pig strains suffering from RP have been reported[79–81], we used an alternative procedure to induce photoreceptor degeneration pharmacologically with systemic administration of the glycolysis inhibitor IAA[59–63]. This resulted in an intense depression of both scotopic and photopic ERG responses. Notably, the depressed ERG responses could be consistently rescued by the injected PPGs, although the resulting ERG waves were smaller than the ERG responses of healthy pigs. This can be due to the limitations of the toxic photoreceptor degeneration model that, in addition to degenerate photoreceptors due to their exceedingly high metabolic rate, is likely to alter the functionality of the inner retina, whose integrity and physiological activity are required for the effects of the prosthetic strategy. Indeed, mild satellitosis of the optic tract along with a mild-to-moderate gliosis of the optic nerve associated with dyskaryosis of glial cells were previously observed after systemic IAA administration in the domestic pig[63].

In conclusion, we have described a type of highly efficient and light-sensitive nanoimplants that can be wirelessly activated by visible light and restore vision in degenerate retinas. Thanks to

https://doi.org/10.1038/s41467-025-63716-4

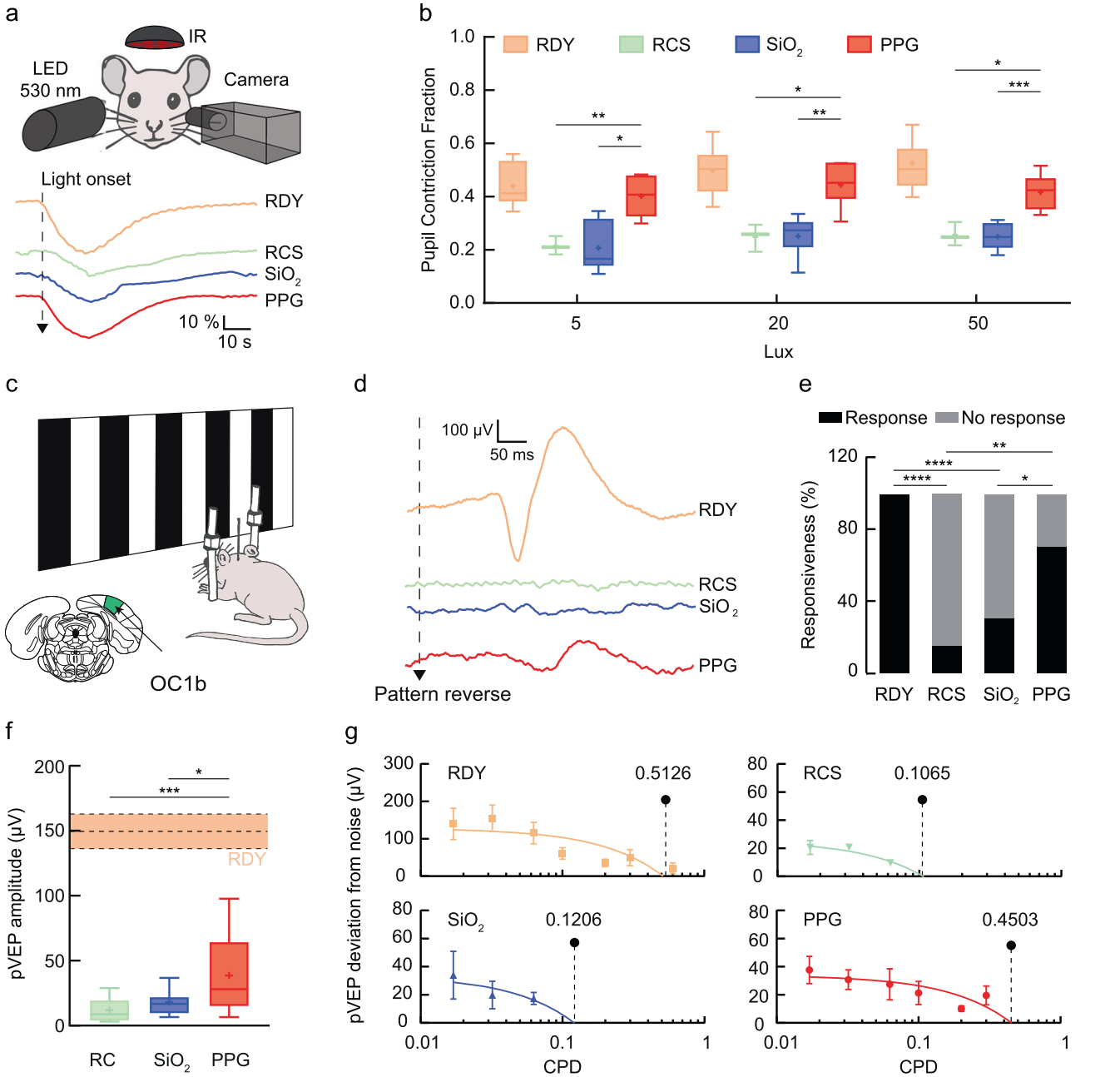

Fig. 5 | Subretinal nanoimplants recover subcortical and cortical light sensitivity. a Top: Schematic representation of pupillary light reflex measurements (20 s, 5-50 lux @ 530 nm). Bottom: Representative traces of the pupillary light reflex recorded at 50 lux in the four experimental groups (n = 12, 3, 9, and 8 rats for RDY, RCS, SiO_2, and PPG, respectively). **b** Box plots of the extent of pupil constriction upon green light stimulation are consistent across various luminances (5 Lux: n = 12, 3, 6, 6, 20 Lux: n = 12,3,7,7, 50 Lux: n = 12,3,9,8 for RDY, RCS, SiO_2, and PPG respectively; p values: RDY vs SiO_2; 0.003; RDY vs RCS: < 0.001; SiO_2 vs PPG: 0.015; PPG vs RCS: 0.008; RDY vs SiO_2: < 0.001; RDY vs RCS: 0.005; SiO_2 vs PPG: 0.002; PPG vs RCS: 0.014; RDY vs SiO_2: < 0.001; RDY vs RCS: < 0.001, SiO_2 vs PPG: < 0.001, PPG vs RCS: 0.017). **c** Schematic representation of the pattern VEP recording setup for the measurement of visual acuity. **d** Representative pattern VEP traces upon contrast reverse (dashed line) of a square wave grating at 0.032 CPD. **e** The percentage of responsiveness (pattern VEP occurrence) to the two lowest spatial frequencies (0.017 and 0.032 CPD) (n = RDY, RCS, SiO2, PPG: 12, 16, 18, 20 animals; RDY vs SiO_2: <0.0001; RDY vs RCS: <0.0001: SiO_2 vs PPG: 0.0217; PPG vs RCS: 0.0031). **f** Box plots of pattern VEP amplitude for the two lowest spatial frequencies are significantly larger in PPG-injected RCS rats than in SiO_2-injected or non-injected animals, although they do not completely recover the pattern VEP amplitude recorded in untreated healthy RDY rats (broken line and orange shaded area representing the mean ± SEM, respectively) (n = 12, 16, 18, and 20 for RDY, RCS, SiO_2, and PPG, respectively). **g** Visual acuity of the four experimental groups, calculated as the X-intercept of the linear regression of pattern VEP amplitude deviation from signal noise vs CPD, reveals a higher visual acuity of PPG-injected animals with respect to SiO_2-injected ones (mean ± SEM from n = 6, 3, 6, and 7 animals for RDY, RCS, SiO_2, and PPG, respectively). *p < 0.05, **p < 0.01, ***p < 0.001, ****p < 0.0001; two-way ANOVA/Tukey's test; (**b**); Fisher's exact test (**e**); Kruskal-Wallis ANOVA/Dunn's tests (**f**).

their enhanced sensitivity, PPGs can harness ambient light without needing external devices such as camera-equipped goggles or light amplifiers and take advantage of the eye's inherent saccadic and micro-saccadic movements to refresh retinal images. The minimally invasive surgical implantation and the wide retinal coverage, potentially restoring the complete visual field, open the avenue in the clinical applications of organic graphene-based materials in degenerative blindness.

https://doi.org/10.1038/s41467-025-63716-4

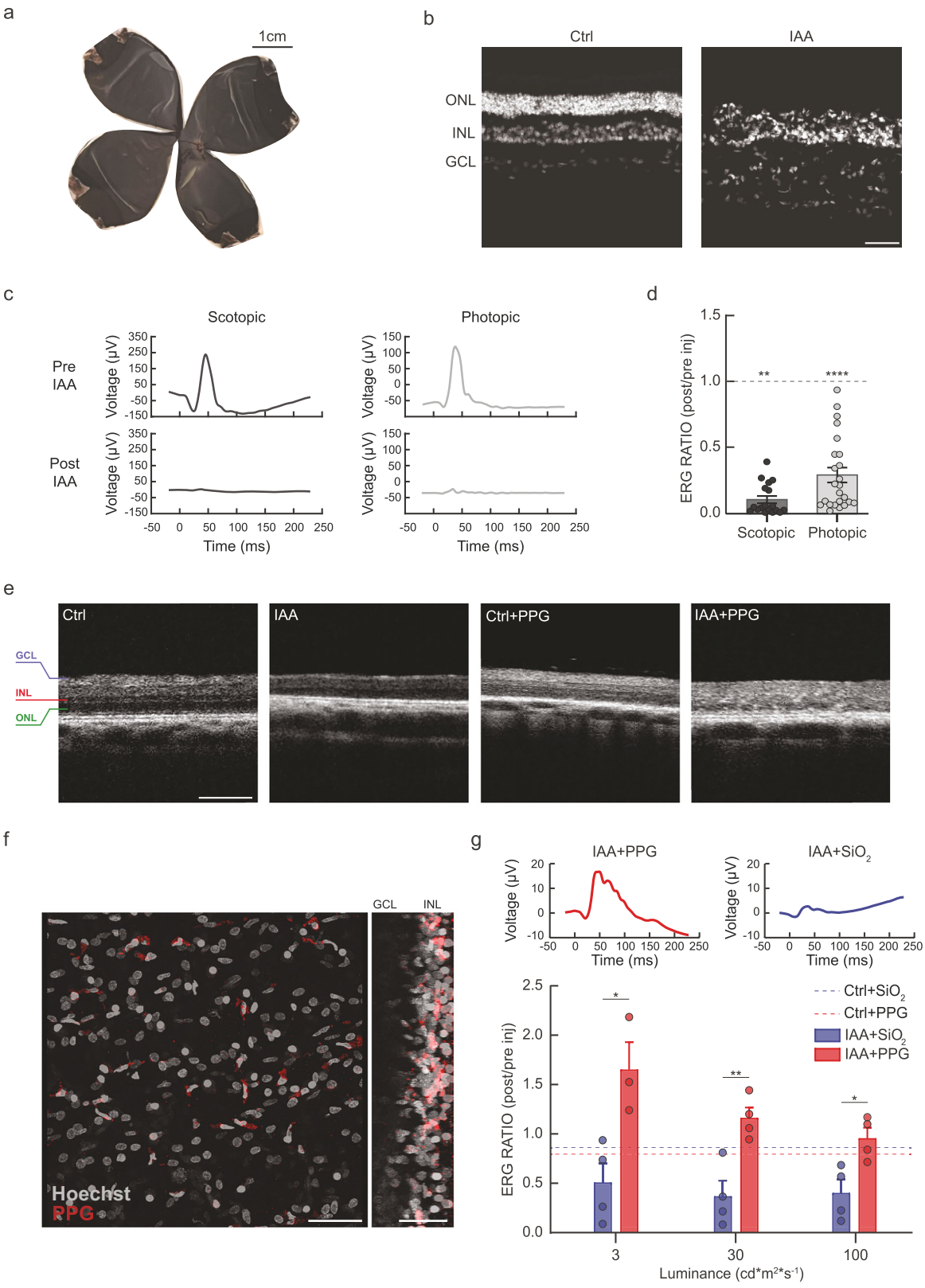

Methods

Nanoparticle synthesis and characterization

P3HT and [6,6]-phenyl C61 butyric acid methyl ester (PCBM) were co-dissolved in THF (P3HT: 10 mg/ml; PCBM: 10 mg/ml) at 50 °C under magnetic stirring (>10 h). Meanwhile, GO powder was dissolved in THF (10 mg/ml), bath sonicated (100 % power, 80 Hz, 20 °C, 2 h), and then ultracentrifuged (18,200 × *g*, 20 °C, 1 h) to collect the supernatant (70 % of total volume) and isolate the fraction of GO flakes with sizes smaller than those of the particles. For PPG, the collected supernatant was added to the co-polymeric blend in a 1:1 v/v ratio, while for PP, pure THF was added to the co-polymeric blend in the same proportions. The ultimate blend was stirred for 2 h at 50 °C in both cases. Nanoimplants were prepared under sterile conditions using the reprecipitation method, with a single rapid injection of the colloidal solution into

Fig. 6 | Subretinal nanoimplants rescue retinal function in a pig model of retinal dystrophy. a Representative picture of a whole-mount, unstained pig retina. Scale bar, 1 cm. **b** Representative images of retinal cross-sections labeled with Hoechst for cell nuclei (white) from pigs that had been treated with either saline (Ctrl) or IAA (12 mg/kg) two weeks before. Retinas from animals injected with IAA reveal a severe disruption of retinal architecture, with a complete loss of photoreceptors in the ONL. Scale bar, 50 μm. **c** Representative scotopic and photopic ERG traces were recorded before and 2 weeks after the photoreceptor lesion with IAA. **d** Mean (± SEM with superimposed individual experimental points) ratio between the ERG b-wave amplitude recorded 2 weeks after the IAA treatment and the corresponding baseline amplitude recorded before the retinal lesion ($n = 3$ luminances x 4 animals x 2 eyes = 24, scotopic: $p = 0.0056$, photopic: $p < 0.0001$). **e** Representative OCT scans of retinas from control saline-treated pigs, IAA-treated pigs, and control and dystrophic pigs subretinally injected with PPGs in the left eye. Scale bar, 250 μm. **f** Representative maximum projection and reconstruction of a retina injected with PPGs (red) obtained by fluorescence confocal microscopy under super-resolution conditions. Scale bar, 50 μm. **g** Top: Representative photopic ERG traces were recorded from the same animal lesioned with IAA, 3 weeks after the subretinal injection of PPGs in the left eye and SiO_2 in the right eye. Bottom: PPG-induced rescue of the ERG b-wave. (Bars represent the mean ± SEM with superimposed individual experimental points) ratio between the ERG b-wave amplitude recorded before and 3 weeks after the subretinal injection of PPGs in the left eye and inert SiO_2 particles in the right eye in either normal pigs or dystrophic pigs that underwent the IAA lesion. PPG-injected dystrophic eyes (solid red) rescue the light-dependent retinal activation with respect to the contralateral eye sham-injected with SiO_2 particles (solid blue). Control animals (red and blue, opaque) showed no ERG change induced by the NP-injection ($n = 4$ and 4 animals for SiO_2 and PPG, respectively; IAA + PPG vs IAA+SiO2, @ 3 $cd*m^2*s^{-1}$: $p = 0.0303$; @ 30 $cd*m^2*s^{-1}$: $p = 0.0080$; @ 100 $cd*m^2*s^{-1}$: $p = 0.0194$). $^*p < 0.05$, $^{**}p < 0.01$, $^{****}p < 0.0001$; one-tailed Student's t-test (d); two-way ANOVA/Sidak's test (**g**).

milli-Q water (previously heated at 50 °C) in a 1:10 v/v ratio. The resulting solution was filtered through a 0.45 μm pore filter to obtain homogeneity and remove aggregates. The colloidal solutions obtained were kept sterile under a laminar flow hood for 2 days to allow the residual organic solvent to evaporate completely. All reagents were provided by Merck (Darmstadt, Germany).

Transmission electron microscopy. Samples were prepared by dropping 5 μl of PPG suspension on copper grids, 150 mesh coated with ultrathin holey carbon film (Sigma-Aldrich, Milano, Italy), and imaged with a JEOL 1011 TEM (100 kV; Tokyo, Japan). The analysis of the sphericity was performed using Fiji.

Dynamic light scattering. Measurements were performed with Zetasizer NanoZS (Malvern Panalytical Ltd, Malvern, UK) by transferring a fresh suspension of particles diluted 1:10 in milli-Q water into a single-use polystyrene half-micro cuvette (DTS 1070, Malvern Panalytical Ltd) with 10 mm path length. The size of diluted particles (1 ml) was determined at 25 °C using a 50-mW laser at 638 nm. The Z-potential of the particles, a hallmark of their aggregation, was measured on the same diluted samples.

Nanoparticle tracking analysis. The concentration of nanoimplants in the suspensions was evaluated using a Nanosight NS300 nanoparticle tracking analysis system (Malvern Panalytical Ltd; laser: 488 nm). The colloidal solution was diluted 1:25 v/v in milli-Q water and loaded in the microfluidic system. A syringe pump maintained a continuous flow of samples through the flow cell (flow rate: 300 μl/min). The estimated concentration of the nanoimplants was around 10^{10} particles/ml.

Photovoltaic properties. To characterize the photovoltaic properties of PPs and PPGs, we performed cyclic voltammetry measurements. The two colloidal solutions were concentrated upon centrifugation 20-fold and dropped onto ITO substrates three consecutive times (2.5-5 μl), intertwined by a 50 °C baking to provide a homogenous surface, and finally glued to a 22-mm diameter glass coverslip. The nanostructured surface, acting as working electrode, was then connected to the recording system with silver glue (~0.5 mm^2 active area). The reference (Ag/AgCl) and counter (Pt) electrodes were dipped in the electrolyte solution (NaCl, 100 mM) to perform current-voltage measurements (voltage range: −0.6 to 0.6 V, scan rate: 100 mV/s, repetitions: 10) with a PalmSens4 potentiostat (PalmSens BV, Houten, The Netherlands). Measurements from all specimens were conducted in the darkness and upon green light excitation (540 nm, 25 mW/mm^2). All analyses were performed using MATLAB (r2023a, The Mathworks, Natick, MA).

Atomic force microscopy. AFM (XE-100, Park Systems Co., Suwon, Korea) measurements were performed to qualitatively characterize the surface of the particle deposition used for the photovoltaic characterization of the material. Measurements were carried out in non-contact mode, scanning a 10 × 10 μm area.

Experimental animals and ethical considerations

The experimental protocols using rats were approved by the Italian Ministry of Health (Authorization # 357/2019-PR). Royal College of Surgeons (RCS) inbred dystrophic rats, together with congenic non-dystrophic (RDY) controls, were kindly provided by Dr. M.M. La Vail (Beckman Vision Center, University of California San Francisco, CA). Rat colonies were bred under standard conditions with *ad libitum* access to food and water under a 12/12 h light/dark cycle. Experimental groups were randomly selected, maintaining a balance of females and males. The use of domestic pigs ($n = 6$ females, ~12 months of age) complied with National and International animal experimentation regulations (D.Lgs 26/2014 implementing the European Directive 2010/63/EU) and was approved by the Italian Ministry of Health (Authorization # 892/2023-PR). These protocols align with the Association for Research in Vision and Ophthalmology's statement regarding the use of animals in ophthalmic and vision research. Commercial hybrid pigs were purchased by a local supplier and transferred to the experimental facility, where they were granted a minimum of 10 days for acclimation. According to their previous social groups, animals were housed in multiple pens, implemented with both edible and durable environmental enrichments, and maintained at 20 ± 4 °C with a 12-hour light/dark cycle. They were fed a weight-based amount of standard growing swine diet (CESAC s.c.a., Conselice, Italy) split into two daily rations and had *ad libitum* access to water. The pigs received a small amount of straw every two days as rooting material. Both the supplier and the experimental facility were accredited as free from Swine Vesicular Disease and Aujeszky disease, with negative serology also for porcine reproductive and respiratory syndrome virus, parvovirus, and circovirus.

Primary cortical neurons

Wild-type C57BL/6 J mice (Charles River, Calco, Italy) were euthanized by CO_2 inhalation and cervical dislocation, and 17/18-day embryos were promptly removed by Cesarean section. Brain cortices were dissected and incubated in 0.125% trypsin for 20 min at 37 °C for enzymatic digestion. Cells were then mechanically dissociated, and the Trypan Blue exclusion assay determined cell viability and number. Neurons were seeded at 40,000 cells on glass coverslips and incubated for up to 10-14 days in Neurobasal medium supplemented with 2% B27, 1% Glutamax, 1% penicillin/streptomycin (all reagents from ThermoFisher Scientific, Monza, Italy).

Live fluorescence imaging. Primary neurons were incubated at 12 days in vitro (DIV), with either PPs or PPGs (1:400 v/v in complete medium) for 5 h, 1, 3, or 6 days before imaging. Cells were stained for 5 min at room temperature with CellMask™ (1 μl/ml, ThermoFisher Scientific) for cell membrane and Hoechst (3.33 μl/ml) for cell nuclei, while P3HT was imaged thanks to its intrinsic fluorescence (λ_{ex}, 561 nm; λ_{em}, 610-710 nm). PP and PPG distribution and co-localization images were acquired with an inverted confocal microscope (SP8, Leica Microsystems GmbH, Wetzlar, Germany). Image analysis was done using ImageJ/Fiji (NIH, Bethesda, MD) and the JACoP plugin.

Patch-clamp on primary neurons. Whole-cell patch-clamp recordings of cortical neurons (14-18 days in vitro, DIV) were performed at room temperature using borosilicate patch pipettes (3.5-5.0 MΩ) and under a GΩ patch seal. The extracellular solution contained (in mM) 135 NaCl, 5.4 KCl, 1 $MgCl_2$, 1.8 $CaCl_2$, 5 HEPES, and 10 Glucose, adjusted to pH 7.4 with NaOH. The intracellular solution contained (in mM): 126 K-Gluconate, 4 NaCl, 1 $MgSO_4$, 0.02 $CaCl_2$, 0.1 EGTA, 10 Glucose, 5 Hepes, 3 ATP-Na, and 0.1 GTP-Na. Recordings were carried out using an EPC10 (HEKA Elektronik, Reutlingen, Germany) amplifier. Measurements of membrane voltage modulation under light stimulation were performed in current-clamp configuration with no current injection (I = 0 pA). Responses were amplified, digitized at 10 or 20 kHz, and stored with Patchmaster V2.73 (HEKA Elektronik). FitMaster v2x90.1 was employed for data analysis, together with Prism 10 (GraphPad Dotmatics, Boston, MA) and OriginPro 9 (OriginLab, Northampton, MA). Photostimulation of neurons was carried out on a Nikon FN1 upright microscope (Nikon Instruments, Tokyo, Japan) by using a combination of 510 nm and 550 nm wavelengths of Spectra X LED light engine (Lumencor, Beaverton, OR) matching the P3HT absorption spectrum (15 mW/mm^2, 50 or 500 ms).

Rat retina electrophysiology

Ex vivo retinal electrophysiology was performed on retinal explants from 10/16-month-old RCS rats, ensuring the total absence of light sensitivity and very low spontaneous activity. Animals were dark-adapted for 30 to 60 min before experiments. Subsequently, they were euthanized under dim red light using CO_2 inhalation followed by cervical dislocation. Eyes were removed, and eyecups were placed in AMES medium (USBiological Life Science, Salem, MA) bubbled with 5% CO_2 and 95% O_2. The sclera and choroid were left in place to allow the ex vivo subretinal injection of the nanoimplants. PPs and PPGs were 20x concentrated and injected at 10^{11} particles/ml. The neural activity of RGCs upon light stimulation was recorded using 60-electrode MEA devices (Multi Channel Systems GmbH, Reutlingen, Germany). Subretinally injected retina pieces were placed RGC-down onto the MEA chips and kept under continuous oxygenated AMES medium perfusion. Signals were acquired at 20 kHz with the MEA1060-INV BC amplifier (Multi Channel Systems) and recorded with the MC Rack software, also used for filtering (HPF, 200 Hz), spike detection (4.5 times SD), and manual sorting. A fiber-coupled Spectra X LED light engine (Lumencor) conveyed light to an inverted Nikon Eclipse Ti (Nikon Instruments Inc.) and optically stimulated retinal explants. To this aim, 25 green light pulses (540 nm) of either 10 or 200 ms were delivered to the retinas for all tested conditions at 10 mW/mm^2, a stimulation intensity consistent with other ex vivo experiments in retinal explants and brain slices[16]. For the analysis, neurons with less than 0.8 Hz basal firing rate (FR) were excluded, together with neurons without a statistically significant light-evoked FR modulation with respect to the pre-pulse. To quantitatively characterize differences in FR across the experimental groups, the post- and pre-stimulation FR ratio was weighted with the photostimulation efficiency, calculated as the percentage of neurons showing a statistically significant FR increase across all 25 stimulation repetitions. The analysis was carried out with OriginPro2020 (OriginLab Corporation), GraphPad Prism 10 (GraphPad Dotmatics), and MATLAB (The Mathworks).

Subretinal injection procedures in the rat

Pink-eyed albino RCS rats (n = 25, 3/4-month-old) of either sex (males: 15 animals, 114 ± 14 days; females: 10 animals, 107 ± 8 days; mean ± SEM) were used for the in vivo experiments. We previously showed that pink-eyed albino RCS rats experience an almost terminal retinal degeneration at 3 months of age, with a complete loss of light perception[34,53]. Animals were anesthetized via intramuscular administration of ketamine (Lobotor, 50 mg/kg) and xylazine (Rompun, 5 mg/kg) and subjected to complete pupil dilation via 1% tropicamide eye drops (Visufarma S.p.A., Roma, Italy). Scissors were employed to perform a conjunctival dissection aligned with the *limbus*, covering ~2 clock hours in the superior-temporal quadrant. Following this, the sclera and choroid were incised about 0.5 mm away from the *limbus*, extending for a 1-mm distance. Subsequently, the retina was delicately separated from the RPE near the incision using either a small amount of viscoelastic material or the tip of surgical scissors. A concentrated colloidal solution of SiO_2 (n = 12, 3-4 months, 8 males: 121 ± 22 days, 4 females: 99 ± 12 days) or PPG (n = 13, 3–4 months, 7 males: 104 ± 17 days, 6 females: 112 ± 11 days) were then introduced via a 38-gauge needle (1-2 μl), ensuring penetration into the subretinal space tangentially to the choroid to detach the retina effectively. Finally, diathermy (utilizing a surgical electrocautery probe) was employed to coagulate the scleral incision, and the conjunctiva was repositioned to cover the wound. The surgical procedures were conducted while maintaining the sterility of the tools and the particle suspension with a Leica ophthalmic surgical microscope (Leica M844, Leica Microsystems GmbH). Following injection, the condition of the retina was assessed using indirect ophthalmoscopy. Tobramycin and dexamethasone eye drops (TobraDex 0.3% + 0.1%) were administered for postoperative prophylaxis.

Behavioral tests in the rat

One month after surgery, rats were subjected to a battery of behavioral tests.

Light-dark box test. The test leverages rodents' innate preference for dark and enclosed spaces to assess light sensitivity and the ensuing anxiety-related behavior. The box has an illuminated and a dark compartment connected by a small aperture. Following 30 min of dark adaptation, each animal was placed in the illuminated area kept at 5 lux and video-recorded for 5 min to measure (i) the escape time from the bright compartment and (ii) the time spent in the dark. Animals that spent more than 1 min in the brighter compartment before transitioning to the dark area for the first time were excluded from the analysis. The number of transitions between the compartments was employed to evaluate the motor activity of the animals. All rats were tested 1 month before and 1 month after surgery[54].

Pupillary light reflex. Two months after the subretinal injection of PPG, PP or SiO_2 particles, rats were dark adapted for 30 min and then maintained in isoflurane anesthesia (Iso-Vet, Piramal Critical Care, Verona, Italy; 2% induction, 2% maintenance in oxygen) for PLR recording. Rats were positioned with an eye (stimulated eye) facing a green LED (530 nm) and the contralateral one (recorded eye) in front of a video camera (1080HDMI; Moticam, Hong Kong, China) and visualized thanks to an infrared LED (780 nm). Both LEDs were obtained from Thorlabs (Newton, NJ). The light stimulation protocol consisted of 20 s of green light exposure at 5, 20, and 50 lux, followed by 60 s of darkness. Changes in pupil size were analyzed from the video recordings using ImageJ (NIH). The ratio between the pupil area before illumination and during the entire stimulation was used to

quantify the PLR. Data analysis was performed with a custom-made MATLAB script[34].

Light-cued classical conditioning. One month after the surgical injection of the nanoimplants (and a corresponding time for the untreated RDY and RCS groups), all groups were subjected to a classical conditioning paradigm (Med Associated Inc., Fairfax, VT) as previously described[56]. The experiment is divided into three phases: conditioning, cue, and context sessions. During conditioning, rats were left 2 min in the dark in the setup chamber to explore the environment freely and then presented with the conditioned stimulus (CS) composed of 5 consecutive flickering blocks (22 lux, 10 light pulses at 5 Hz, 50% duty cycle) interspersed with 2 s of dark repeated 7 times every 60 s. The last flickering stimulus of each repetition was associated with a foot shock of 0.5 mA as the unconditioned stimulus (US). The US-CS associative learning was quantified by the freezing time of the animals during the experimental protocol. The cued session performed the day after the conditioning session, was employed to evaluate the CS-US association while minimizing the chamber-US association. To achieve this, the environment was altered by covering the grid floor with a smooth white plastic sheet, replacing the arena with black and white striped walls, introducing a new aromatic odor (Vanillin, Sigma-Aldrich, USA), and adding two wired cups to the chamber. After 5 min of habituation in the apparatus, each animal underwent a 2-min period in the dark followed by 3 min continuous CS presentation (2.5-22 lux, 45 flickering blocks as described above interspersed by 2 s of darkness). Freezing behavior was quantified during the dark period, and the CS presentation was used to assess light stimulus perception. Finally, the day after the cue session, animals were subjected to the context session that was taking place in the same chamber as the conditioning session but in the absence of either CS or US. During this phase each rat was kept in the chamber for 5 min while recording the freezing behavior. Before each test session, rats underwent 1 h of dark adaptation, and all experiments were conducted under dark conditions. Freezing behavior during each test session was expressed as the percentage of time spent freezing (freezing time/total session time). Freezing time trends were analyzed by monitoring the motion index (MI) provided by Video-Freeze 2.25 software. The motion index was updated at the camera frame rate (30 Hz) and thresholded considering "*freezing*" when MI = 0 and "*motion*" when MI > 0. This way, freezing events were detected every 33 ms. Time histograms of freezing events (bin = 3 s) were then normalized for the average occurrence of freezing events during darkness (2 min). Statistical analysis was performed on freezing events trends during light, considering the normalized average frequency of freezing events.

VEP recordings in the rat

Animals from each experimental group were subjected to in vivo electrophysiological recordings to characterize patterned VEPs as previously described[33,34]. The animals were anesthetized via intramuscular administration of ketamine (50 mg/kg) and xylazine (5 mg/kg) and placed in a stereotaxic frame (Stoelting, Wood Dale, IL). Anesthesia was maintained stable during the whole course of the experiment, as well as body temperature (36-37 °C). A hole was drilled into the skull corresponding to the binocular portion of V1 (OC1b) ~4.8–5 mm from lambda (the intersection between the sagittal and lambdoid sutures), after which the dura mater was delicately removed to expose the brain surface. A glass micropipette (2–4 MΩ), filled with 3 M NaCl solution (Sigma-Aldrich), was carefully inserted down to 400 μm in depth. Throughout the experiment, both eyes were moistened with a saline solution (0.9% NaCl) and secured open using adjustable metal rings. Visual acuity was evaluated by presenting to the animals a vertical square wave contrast-reversing grating at randomized different spatial frequencies (100% contrast, 0.017-1 cycles per degree, CPD). Stimuli were controlled by a custom-made MATLAB application enabling the design and presentation using a ViSaGe MKII (Cambridge Research Systems, Rochester, UK). All stimuli were presented with a CRT monitor placed at 25 cm from the animal eyes (120 cd/m^2, SpectroCAL MKII Spectroradiometer, Cambridge Research Systems). All signals were amplified and band-pass filtered (0.1-100 Hz) by a Neurolog system (Digitimer, Hertfordshire, UK). Digitization of the signal was handled by a Data Acquisition system (DAQ, NI USB-6251, National Instruments, Austin, TX), and acquisition, storing, and analysis were handled by the same custom-made MATLAB application used to design the visual stimulation. All traces extracted in the time window around the reverse of light stimulation, whose SD value exceeded 120% of the mean SD value of all extracted windows, were excluded. VEP peak detection threshold was set 2-fold the SD of the noise. Visual acuity was then extrapolated from the X-intercept resulting from the linear regression of the VEP amplitudes corrected for the standard deviation of the average response to the maximum spatial frequency (1 CPD) *versus* the tested spatial frequencies.

IAA-induced retinal dystrophy

It has been shown that a systemic injection of a low dose of IAA, harmless to other tissues, triggers photoreceptor degeneration due to an exceedingly high rate of glycolytic activity of photoreceptors, resulting in a combined rod-cone degeneration that is particularly severe in the visual streak[62,63]. Two weeks before subretinal surgery and baseline electrophysiological assessments, animals belonging to the dystrophic group under general anesthesia were administered intravenously with 12 mg/kg of freshly solubilized IAA (in sterile saline) via a catheter placed in the auricular vein. After the treatment, pigs were strictly monitored for 30 min before being woken up and followed up to exclude the presence of systemic toxicity of the treatment. Blood samples were collected to evaluate haemato-chemical parameters. In previous studies, we found that photoreceptor degeneration starts to be detectable 2 weeks after the injection and stabilizes between 4 and 12 weeks, with massive thinning of the photoreceptor layer associated with the disappearance of scotopic and photopic ERG potentials contributed by rods and cones, respectively.

Subretinal surgery in the pig

Two weeks after the IAA lesion, degenerated pigs, along with normal pig controls, were sedated with an intramuscular (IM) injection of Tiletamine-Zolazepam (Zoletil; 5 mg/kg). After 15 min, general anesthesia was initiated using 8% sevoflurane (SevoFlo), delivered through a mask in a 1:1 oxygen/air mixture. The same halogenated agent was used for anesthesia maintenance at 3% following orotracheal intubation. Lactated Ringer's solution was administered at 10 ml/kg/h via the auricular vein (left ear). Anesthesia was maintained at 3% following orotracheal intubation. Lactated Ringer's solution was administered at 10 ml/kg/h via the auricular vein (left ear). During the anesthesia, vital signs were closely monitored, including heart rate, non-invasive blood pressure (NIBP), peripheral capillary oxygen saturation (SpO_2), and carbon dioxide (CO_2) levels. Local anesthesia was achieved by applying oxybuprocaine hydrochloride eye drops (Novesina 0.4%). The periocular region was shaved and disinfected using Povidone-Iodine 10%; then, a sterile drape was placed over the area. The eye was opened using a speculum, and two 23-gauge and one 20-gauge trocar were inserted 1.5 mm from the limbus. A chandelier light was set up to assist with the bimanual surgery. A posterior vitreous detachment was created using active suction via the cutter, followed by a vitrectomy while ensuring careful protection of the lens. To separate the posterior retina from the RPE, a balanced salt solution (Alcon Laboratories, Geneva, Switzerland) was injected into the subretinal space through a 41-gauge subretinal cannula connected to an automated pump. This injection was adjusted to detach the temporal side of the visual streak. A 1.5-mm mid-peripheral retinotomy was performed using scissors (DORC International, Zuidland, The Netherlands). The needle connected with the perfusion pump for the administration of the colloidal

suspension of nanoimplants (PPGs in the left eye and SiO_2 in the right eye) was placed into the vitreous cavity and was then maneuvered into the subretinal space. Perfluorocarbon liquid was injected into the vitreous cavity to effectively cover the retinotomy and reattach the retina. Laser endo-photocoagulation was carried out around the edge of the retinotomy. A fluid/air exchange process was done, after which the trocars were taken out, and the sclerotomies were closed using Vicryl 8-0 sutures. An isovolumic mixture of sulfur hexafluoride (SF6) gas was utilized as the final tamponade. Following surgery, all animals were given intra-conjunctival administration of triamcinolone acetonide (Kenacort; 40 mg per eye) along with fluocinolone acetonide/neomycin eye drops (Iridex).

Optical coherence tomography in the pig

Pigs were anesthetized as previously described, and their pupils were dilated using 1% tropicamide eye drops (Visumidriatic) before image acquisition. Spectral-domain OCT was performed with the Optovue iVue device (Visionix, Lombard, IL), which utilizes light at a wavelength of 840 ± 10 nm and delivers a power of 750 μW at the pupil. The depth resolution in tissue is 5 μm, while the transverse resolution is 15 μm. Each image captured a 6 ×6 mm area centered on the fovea, with a scan rate of 26,000 A-scans per second and comprised 256 to 1,024 A-scans per frame.

ERG recordings in the pig

The electrophysiological analysis in pigs was conducted before and after the IAA lesion and after the surgical implantation procedure, with the animals under general anesthesia, as per the protocol described in Supplementary Fig. 4[82]. Pupils were dilated using 1% tropicamide eye drops (Visumidriatic). Two drops of oxybuprocaine hydrochloride (Novesina) were applied for local anesthesia. A Barraquer blepharostat was used to keep the eyes in a central and stable position, secured by two stay sutures. Corneal disposable contact lens electrodes (ERGjet, Universo Plastique, La Chaux-de-Fonds, Switzerland) served as the active electrodes, while dermal needle electrodes used as reference and ground were placed under the ipsilateral eyelid and aborally on the snout during full-field electroretinography (ff-ERG). A drop of benzalconium chloride polyacrylic acid gel (Lacrinorm) was applied to the inner surface of the lens electrodes to protect the cornea and ensure good electrical contact. Settings were adjusted precisely for the swine species following the International Society for Clinical Electrophysiology of Vision (ISCEV) standards for ff-ERGs[82]. We performed ff-ERG recordings using both scotopic and photopic protocols to evaluate the extent of the IAA lesion and to compare retinal activity after surgical implantation of PPGs (left eye) and the inert SiO_2 (right eye) within individual animals. Briefly, ff-ERG recordings were filtered using a 2–500 Hz band-pass FFT filter. The adaptation/background light luminance was set at 30 cd/m² for 10 min. A Ganzfeld dome produced the ff-ERG stimuli, with the stimulus luminance set at 3, 30, and 100 cd/s/m² and an inter-stimulus interval of 1.1 Hz. We measured the amplitude (μV) from the "a" to "b" waves as, respectively, the minimal and maximal deflection following the flashlight. The data were amplified and acquired using WinAverager software. All electrophysiological data were acquired and amplified using the Retimax system (C.S.O. srl, Florence, Italy). Both eyes were tested separately, with the opposite eye covered to prevent light exposure during the recordings. Each experimental session, including the animal preparation, lasted ~2 h. The animals were gently recovered from anesthesia at the end of the electrophysiology sessions. The electrodes, sutures, and blepharostat were removed, and an ophthalmic ointment (Colbiocin) containing chloramphenicol (10 mg)/sodium colistimethate (180,000 U.I.)/tetracycline (5 mg) was applied to the conjunctiva. The animals were then moved to a dark and quiet room, and the orotracheal tube was removed once the swallowing reflex returned. Pigs fully recovered from anesthesia within 2 h and were returned to their original pens.

Retina histochemistry

Eyes were carefully removed and marked for temporal-nasal orientation for histology. Subsequently, the eyes were fixed in a 4% paraformaldehyde solution (PFA, Sigma-Aldrich) in 0.1 M phosphate-buffered saline (PBS) overnight and then washed with 0.1 M PBS (3 times for 10 min).

Whole-mount rat retinal preparations. The eyecup was incised with a blade scalpel blade, cutting it into 4–5 petals to flatten the retina. The whole mount was incubated in free-floating for 30 min with bisbenzimide (1:300) for nuclear labeling and then rinsed three times with 0.1 M PBS. The whole mount was placed between two coverslips (60 × 40 mm), and the PPG distribution was assessed by confocal microscopy of the intrinsic fluorescence of P3HT. Retinal coverage and total area of PPGs were assessed by analyzing whole-mount retina tile scan mosaics using an SP8 confocal microscope with a 10x objective (Leica Microsystems). The total area of PPGs was evaluated through binarized z-max projections of the P3HT fluorescence. To generate the PPG mask, each z-max projection underwent several processing steps using ImageJ, namely: (i) application of a median filter (2 pixels); (ii) use of a double-direction Sobel edge detector filter ([1 2 1; 0 0 0; -1 -2 -1], [1 0 -1; 2 0 -2; 1 0 -1]); (iii) thresholding using the Shanbhag method; (iv) binarization; (v) closing operation; (vi) filling holes; and (vii) opening operation. The total area of the binary masks was calculated to calculate the PPG area. For coverage calculation, the masks were imported into a custom MATLAB script designed to manually track the more distal PPGs relative to the optic nerve. Each mask was overlaid onto a radial grid centered on the optic nerve with a resolution of 4 degrees. The most distal object in each sector was identified as the maximum spread distance of the PPGs. These distal points were connected, and the resulting mask was combined with the whole retina mask using the AND operator. The coverage percentage was then calculated as the ratio of the area represented by this mask to the total area of the whole retina mask.

To examine the distribution of PPGs throughout the whole-mount retinas, each mask from individual explants was aligned using the petal corresponding to the injection site. Next, a grid was established by intersecting a radial grid (10 degrees resolution) and concentric circular *anuli* spaced 350 μm apart. The number of objects and the density of PPGs per unit area were determined for each sector created by these intersections.

Rat retina immunohistochemistry. After removal of the cornea, iris, and lens, eyecups were cryoprotected using a 15–30 % sucrose gradient until precipitation, embedded in Tissue-Tek O.C.T. (Qiagen, Ilden, Germany), frozen in dry ice, and cryo-sectioned at 25-μm thickness using a CM1860 cryostat (Leica Microsystems). Sections were collected on gelatine- and polylysine-coated (Sigma-Aldrich) glass slides and stored at −20 °C until further processing. For morphological analyses, sections were washed 3 times in 0.1 M PBS to remove any trace of freezing medium and then incubated with 10 % normal goat serum (NGS, Sigma-Aldrich) to block non-specific antibody binding. Primary antibodies were diluted in 0.05 % Triton X-100 in 0.1 M PBS and incubated overnight at 4 °C. To label Müller cells/astrocytes, microglia and microglia activation, retinal sections were incubated with anti-GFAP (1:200, G3893, Sigma-Aldrich), anti-Iba-1 (cat# 019-19741; 1:300; Fujifilm Wako, Neuss, Germany) and anti- rat CD68 (1:250, MCA341R, BioRad Antibodies), respectively. To remove the excess primary antibodies, samples were rinsed 3 times in 0.1 M PBS and then incubated for 1 h at room temperature with Alexa Fluor 488 (1:100 diluted in 0.05 % Triton X-100 in 0.1 M PBS), Alexa Fluor 647 (1:500, A21245, invitrogen) -conjugated secondary antibodies, and bisbenzimide nuclear labeling (1:300; Sigma-Aldrich). Samples were rinsed 3 times in 0.1 M PBS, dried, and mounted with VectaMount (cat# H-5501-60; Vector Laboratories, Newark, CA) onto glass coverslips.

Retinal sections were imaged using a Leica SP8 confocal microscope (Leica Microsystems). PPGs were visualized by acquiring the intrinsic P3HT fluorescence using specific excitation and emission wavelengths (λ_{ex}, 561 nm; λ_{em}, 610–710 nm). Morphometric analyses of the retina were conducted by imaging the central fields of both temporal and nasal regions for each retinal slice, with consistent acquisition parameters maintained throughout the imaging sessions for comparison purposes. GFAP integrated density for both temporal and nasal areas was determined by averaging measurements from three regions of interest (ROIs, 30 × 30 μm) in the ONL, IPL, and GCL, respectively. GFAP was quantified as the ratio between the integrated density of the ONL and that of all retinal layers (ONL/ONL + IPL + GCL). Sholl analysis was performed by isolating and binarizing single microglial cells at the ONL level, with the soma diameter serving as the starting circle (start: 20 μm, step size: 5 μm).

Pig retina histochemistry. The pig's enucleated eyes were fixed and dissected to obtain whole mounts using the same procedure described for the rat. Unlike the previous method, retinas were isolated from the RPE and the sclera, whose large size prevented proper tissue cutting. The individual petals were then frozen, sectioned with a cryostat, and immunolabeled with bisbenzimide following the previous method used for rats.

Statistical analysis

The sample size needed for the planned experiments (n) was predetermined using the G*power software for the ANOVA test by considering an effect size = 0.25-0.40 with (type-I error) = 0.05, and 1-ß (type-II error) = 0.9, based on similar experiments and preliminary data. Experimental data are expressed either as means ± SEM (bar plots) or as box plots (center line, median; square symbol, mean; box limits, 25^{th}–75^{th} percentiles; whisker length, Tukey method), with n as the number of neurons (in vitro/ex vivo experiments) or individual animals (in vivo experiments). The normal distribution of experimental data was assessed using either the D'Agostino-Pearson's or the Shapiro-Wilk's normality test. The unpaired/paired Student's *t*-test or Wilcoxon's signed-rank test was used to compare two sample groups, depending on sample pairing and normality distribution. Two-tailed tests have been employed for all statistical evaluations, unless specified otherwise in the figure legend. One- or two-way ANOVA was used to compare more than two normally distributed sample groups, followed by Tukey's, Holm-Šídák post hoc multiple comparison test. The one-way Kruskal-Wallis ANOVA was used to compare more than two non-normally distributed sample groups, followed by Dunn's multiple comparison test. To perform the statistical analysis of contingency tables, Fisher's or chi-square exact test was used. The threshold for statistical significance was set at $p < 0.05$. Statistical analysis was performed using OriginPro (v2020 SR1; OriginLab Corporation) and GraphPad Prism (v8.3.0; GraphPad Dotmatics).

Reporting summary

Further information on research design is available in the Nature Portfolio Reporting Summary linked to this article.

Data availability

All data supporting the findings of this study are available within the article and its supplementary files. Any additional requests for information can be directed to and will be fulfilled by the corresponding authors. Source data are provided with this paper.

References

1. Pascolini, D. & Mariotti, S. P. Global estimates of visual impairment: 2010. *Br. J. Ophthalmol.* **96**, 614–618 (2012).
2. Provis, J. M., Penfold, P. L., Cornish, E. E., Sandercoe, T. M. & Madigan, M. C. Anatomy and development of the macula: specialisation and the vulnerability to macular degeneration. *Clin. Exp. Optom.* **88**, 269–281 (2005).
3. Fabrício, D., de, Chagas, M. & Diniz, M. H. N. B. S. Frailty and cognitive decline. *Transl. Res* **221**, 58–64 (2020).
4. Cross, N., van Steen, C., Zegaoui, Y., Satherley, A. & Angelillo, L. Retinitis Pigmentosa: burden of disease and current unmet needs. *Clin. Ophthalmol.* **16**, 1993–2010 (2022).
5. Masland, R. H. The neuronal organization of the retina. *Neuron* **76**, 266–280 (2012).
6. Parmeggiani, F. et al. Retinitis pigmentosa: genes and disease mechanisms. *Curr. Genomics* **12**, 238–249 (2011).
7. Berdeaux, G. H., Nordmann, J. P., Colin, E. & Arnould, B. Vision-related quality of life in patients suffering from age-related macular degeneration. *Am. J. Ophthalmol.* **139**, 271–279 (2005).
8. Yonekawa, Y. & Kim, I. K. Clinical characteristics and current treatment of age-related macular degeneration. *Cold Spring Harb Perspect Med* **5**, a017178 (2014).
9. Li, J. Q. et al. Prevalence and incidence of age-related macular degeneration in Europe: a systematic review and meta-analysis. *Br. J. Ophthalmol.* **104**, 1077–1084 (2020).
10. Scholl, H. P. N. et al. Emerging therapies for inherited retinal degeneration. *Sci. Transl. Med.* **8**, 368rv6 (2016).
11. Cehajic-Kapetanovic, J., Singh, M. S., Zrenner, E. & MacLaren, R. E. Bioengineering strategies for restoring vision. *Nat. Biomed. Eng.* **7**, 387–404 (2023).
12. Trapani, I., Banfi, S., Simonelli, F., Surace, E. M. & Auricchio, A. Gene therapy of inherited retinal degenerations: prospects and challenges. *Hum. Gene Ther.* **26**, 193–200 (2015).
13. Yalla, G. R. & Kuriyan, A. E. Cell therapy for retinal disease. *Curr. Opin. Ophthalmol.* **35**, 178–184 (2024).
14. Lindner, M., Gilhooley, M. J., Hughes, S. & Hankins, M. W. Optogenetics for visual restoration: From proof of principle to translational challenges. *Prog. Retin. Eye Res.* **91**, 101089 (2022).
15. Bloch, E., Luo, Y. & da Cruz, L. Advances in retinal prosthesis systems. *Ther. Adv. Ophthalmol.* **11**, 1–16 (2019).
16. Lanzani, G. et al. Nanotechnology for vision restoration. *Nat. Rev. Bioeng.* **2**, 829–848 (2024).
17. Nair, D. S. R. & Thomas, B. B. Stem cell-based treatment strategies for degenerative diseases of the retina. *Curr. Stem Cell Res Ther.* **17**, 214–225 (2022).
18. Sahel, J. A. et al. Partial recovery of visual function in a blind patient after optogenetic therapy. *Nat. Med* **27**, 1223–1229 (2021).
19. Qian, X. et al. Noninvasive ultrasound retinal stimulation for vision restoration at high spatiotemporal resolution. *BME Front* **2022**, 9829316 (2022).
20. Cadoni, S. et al. Ectopic expression of a mechanosensitive channel confers spatiotemporal resolution to ultrasound stimulations of neurons for visual restoration. *Nat. Nanotechnol.* **18**, 667–676 (2023).
21. Weiland, J. D., Cho, A. K. & Humayun, M. S. Retinal prostheses: Current clinical results and future needs. *Ophthalmology* **118**, 2227–2237 (2011).
22. Stingl, K. et al. Interim Results of a Multicenter Trial with the New Electronic Subretinal Implant Alpha AMS in 15 Patients Blind from Inherited Retinal Degenerations. *Front Neurosci.* **11**, 445 (2017).
23. Lorach, H. et al. Photovoltaic restoration of sight with high visual acuity. *Nat. Med* **21**, 476–482 (2015).
24. Ghezzi, D. et al. A polymer optoelectronic interface restores light sensitivity in blind rat retinas. *Nat. Photonics* **7**, 400–406 (2013).
25. Antognazza, M. R. et al. Characterization of a polymer-based, fully organic prosthesis for implantation into the subretinal space of the rat. *Adv. Healthc. Mater* https://doi.org/10.1002/adhm.201600318 (2016).

26. Maya-Vetencourt, J. F. et al. A fully organic retinal prosthesis restores vision in a rat model of degenerative blindness. *Nat Mater* https://doi.org/10.1038/nmat4874 (2017).
27. DiFrancesco, M. L. et al. A hybrid P3HT-Graphene interface for efficient photostimulation of neurons. *Carbon N Y* https://doi.org/10.1016/j.carbon.2020.02.043 (2020).
28. Maya-Vetencourt, J. F. et al. Biocompatibility of a conjugated polymer retinal prosthesis in the domestic pig. *Front Bioeng. Biotechnol.* **8**, 1–19 (2020).
29. Francia, S. et al. P3ht-graphene device for the restoration of visual properties in a rat model of retinitis pigmentosa. *Adv. Mater. Technol.* **8**, 2201467 (2023).
30. Lee, D. Y., Lorach, H., Huie, P. & Palanker, D. Implantation of modular photovoltaic subretinal prosthesis. *Ophthalmic Surg. Lasers Imaging Retin.* **47**, 171–174 (2016).
31. Vagni, P. et al. POLYRETINA restores light responses in vivo in blind Göttingen minipigs. *Nat Commun* **13**, 3678 (2022).
32. Wang, B. Y. et al. Electronic photoreceptors enable prosthetic visual acuity matching the natural resolution in rats. *Nat Commun* **13**, 6627 (2022).
33. Maya-Vetencourt, J. F. et al. Subretinally injected semiconducting polymer nanoparticles rescue vision in a rat model of retinal dystrophy. *Nat. Nanotechnol.* https://doi.org/10.1038/s41565-020-0696-3 (2020).
34. Francia, S. et al. Light-induced charge generation in polymeric nanoparticles restores vision in advanced-stage retinitis pigmentosa rats. *Nat. Commun.* **13**, 1–19 (2022).
35. Rommelfanger, N. J. & Hong, G. Conjugated polymers enable a liquid retinal prosthesis. *Trends Chem.* **2**, 961–964 (2020).
36. Chiaravalli, G. et al. The light-dependent pseudo-capacitive charging of conjugated polymer nanoparticles coupled with the depolarization of the neuronal membrane. *Phys. Chem. Chem. Phys.* **26**, 47–56 (2023).
37. Mosconi, E. et al. Surface polarization drives photoinduced charge separation at the P3HT/water interface. *ACS Energy Lett.* **1**, 454–463 (2016).
38. Ghezzi, D. et al. A hybrid bioorganic interface for neuronal photoactivation. *Nat. Commun.* **2**, 166 (2011).
39. Fadeel, B. et al. Safety assessment of graphene-based materials: focus on human health and the environment. *ACS Nano* **12**, 10582–10620 (2018).
40. Lin, H. et al. Environmental and health impacts of graphene and other two-dimensional materials: a graphene flagship perspective. *ACS Nano* **18**, 6038–6094 (2024).
41. Amollo, T. A., Mola, G. T. & Nyamori, V. O. High-performance organic solar cells utilizing graphene oxide in the active and hole transport layers. *Sol. Energy* **171**, 83–91 (2018).
42. Muchuweni, E., Martincigh, B. S. & Nyamori, V. O. Organic solar cells: current perspectives on graphene-based materials for electrodes, electron acceptors and interfacial layers. *Int J. Energy Res* **45**, 6518–6549 (2021).
43. Nguyen, D. C. T., Mai, V. D., Tran, V. H., Vu, V. P. & Lee, S. H. Use of modified PEDOT:PSS/Graphene oxide dispersions as a hole transport layer for inverted bulk-heterojunction organic solar cells. *Org. Electron* **100**, 106388 (2022).
44. Lee, R. H., Huang, J. L. & Chi, C. H. Conjugated polymer-functionalized graphite oxide sheets thin films for enhanced photovoltaic properties of polymer solar cells. *J. Polym. Sci. B Polym. Phys.* **51**, 137–148 (2013).
45. Zheng, F., Xu, W. L., Jin, H. D., Hao, X. T. & Ghiggino, K. P. Charge transfer from poly(3-hexylthiophene) to graphene oxide and reduced graphene oxide. *RSC Adv.* **5**, 89515–89520 (2015).
46. Zheng, F. et al. Poly(3-hexylthiophene) coated graphene oxide for improved performance of bulk heterojunction polymer solar cells. *Org. Electron* **44**, 149–158 (2017).
47. Colom, E. et al. Graphene oxide: key to efficient charge extraction and suppression of polaronic transport in hybrids with poly (3-hexylthiophene) nanoparticles. *Chem. Mater.* **35**, 3522–3531 (2023).
48. Tullii, G. et al. Bimodal functioning of a mesoporous, light sensitive polymer/electrolyte interface. *Org. Electron* **46**, 88–98 (2017).
49. DiFrancesco, M. L. et al. Neuronal firing modulation by a membrane-targeted photoswitch. *Nat Nanotechnol* https://doi.org/10.1038/s41565-019-0632-6 (2020).
50. LaVail, M. M., Sidman, R. L. & Gerhardt, C. O. Congenic strains of RCS rats with inherited retinal dystrophy. *J. Hered.* **66**, 242–244 (1975).
51. Strettoi, E., Pignatelli, V., Rossi, C., Porciatti, V. & Falsini, B. Remodeling of second-order neurons in the retina of rd/rd mutant mice. *Vis. Res* **43**, 867–877 (2003).
52. Pfeiffer, R. L., Marc, R. E. & Jones, B. W. Persistent remodeling and neurodegeneration in late-stage retinal degeneration. *Prog Retin Eye Res* **74**, 100771 (2020).
53. Suematsu, N., Sato, A. Y., Kimura, A., Shimegi, S. & Soma, S. Perceptual visual acuity declines with age in a rat model of retinitis pigmentosa while light perception is maintained. *Invest Ophthalmol Vis. Sci.* **66**, 31 (2025).
54. Bourin, M. & Hascoët, M. The mouse light/dark box test. *Eur. J. Pharm.* **463**, 55–65 (2003).
55. Newton, J. R., Ellsworth, C., Miyakawa, T., Tonegawa, S. & Sur, M. Acceleration of visually cued conditioned fear through the auditory pathway. *Nat. Neurosci.* **7**, 968–973 (2004).
56. Ivashkina, O. I., Toropova, K. A., Roshchina, M. A. & Anokhin, K. V. Acquisition of a Conditioned Fear Reaction to a Light Stimulus in Mice: Comparison with Learning in Response to a Sound Stimulus. *Neurosci. Behav. Physiol.* **47**, 994–998 (2017).
57. Lind, N. M. et al. The use of pigs in neuroscience: modeling brain disorders. *Neurosci. Biobehav Rev.* **31**, 728–751 (2007).
58. Barone, F. et al. Behavioral Assessment of Vision in Pigs. *J. Am. Assoc. Lab Anim. Sci.* **57**, 350–356 (2018).
59. Scott, P. A., Kaplan, H. J. & Sandell, J. H. Anatomical evidence of photoreceptor degeneration induced by iodoacetic acid in the porcine eye. *Exp. Eye Res* **93**, 513–527 (2011).
60. Wang, W. et al. Selective rod degeneration and partial cone inactivation characterize an iodoacetic acid model of swine retinal degeneration. *Invest Ophthalmol. Vis. Sci.* **52**, 7917–7923 (2011).
61. Noel, J. M. et al. Iodoacetic acid, but not sodium iodate, creates an inducible swine model of photoreceptor damage. *Exp. Eye Res* **97**, 137 (2012).
62. Elmi, A. et al. 1H NMR Spectroscopy Characterization of Porcine Vitreous Humor in Physiological and Photoreceptor Degeneration Conditions. *Invest Ophthalmol. Vis. Sci.* **60**, 741–747 (2019).
63. Barone, F. et al. The porcine iodoacetic acid model of retinal degeneration: Morpho-functional characterization of the visual system. *Exp Eye Res* **193**, (2020).
64. Orbach, G. et al. Visual Impairment in Pre-Clinical Models of Mild Traumatic Brain Injury. *J. Neurotrauma* **41**, 1842–1852 (2024).
65. Brouwer, A. H. et al. Electroretinogram abnormalities in non-infectious uveitis often persist. *Acta Ophthalmol.* **98**, 627–633 (2020).
66. Chen, J., Patil, S., Seal, S. & McGinnis, J. F. Rare earth nanoparticles prevent retinal degeneration induced by intracellular peroxides. *Nat. Nanotechnol.* **1**, 142–150 (2006).
67. Cupini, S. et al. Platinum Nanozymes Counteract Photoreceptor Degeneration and Retina Inflammation in a Light-Damage Model of Age-Related Macular Degeneration. *ACS Nano* **17**, 22800–22820 (2023).
68. Huang, H., Delikanli, S., Zeng, H., Ferkey, D. M. & Pralle, A. Remote control of ion channels and neurons through magnetic-field heating of nanoparticles. *Nat. Nanotechnol.* **5**, 602–606 (2010).

69. Li, W. et al. Remote modulation of neural activities via near-infrared triggered release of biomolecules. *Biomaterials* https://doi.org/10.1016/j.biomaterials.2015.06.041 (2015).
70. Carvalho-de-Souza, J. L., Pinto, B. I., Pepperberg, D. R. & Bezanilla, F. Optocapacitive Generation of Action Potentials by Microsecond Laser Pulses of Nanojoule Energy. *Biophys J* https://doi.org/10.1016/j.bpj.2017.11.018 (2018).
71. Nelidova, D. et al. Restoring light sensitivity using tunable near-infrared sensors. *Science (1979)* https://doi.org/10.1126/science.aaz5887 (2020).
72. Chen, S. et al. Near-infrared deep brain stimulation via upconversion nanoparticle–mediated optogenetics. *Science (1979)* **359**, 679–684 (2018).
73. Ma, Y. et al. Mammalian Near-Infrared Image Vision through Injectable and Self-Powered Retinal Nanoantennae. *Cell* **177**, 243–255.e15 (2019).
74. Chiacchiaretta, M. et al. Graphene Oxide Upregulates the Homeostatic Functions of Primary Astrocytes and Modulates Astrocyte-to-Neuron Communication. *Nano Lett.* **18**, 5827–5838 (2018).
75. Bramini, M. et al. Interfacing graphene-based materials with neural cells. *Front Syst Neurosci* **12**, 12 (2018).
76. Jones, B. W. et al. Retinal remodeling triggered by photoreceptor degenerations. *J. Comp. Neurol.* **464**, 1–16 (2003).
77. Peng, Y. W., Senda, T., Hao, Y., Matsuno, K. & Wong, F. Ectopic synaptogenesis during retinal degeneration in the royal college of surgeons rat. *Neuroscience* **119**, 813–820 (2003).
78. Lee, J. Y., Care, R. A., Della Santina, L. & Dunn, F. A. Impact of Photoreceptor Loss on Retinal Circuitry. *Annu Rev. Vis. Sci.* **7**, 105–128 (2021).
79. Petters, R. M. et al. Genetically engineered large animal model for studying cone photoreceptor survival and degeneration in retinitis pigmentosa. *Nat. Biotechnol.* **15**, 965–970 (1997).
80. Sommer, J. R., Wong, F. & Petters, R. M. Phenotypic stability of Pro347Leu rhodopsin transgenic pigs as indicated by photoreceptor cell degeneration. *Transgenic Res* **20**, 1391–1395 (2011).
81. Ross, J. W. et al. Generation of an inbred miniature pig model of retinitis pigmentosa. *Invest Ophthalmol. Vis. Sci.* **53**, 501–507 (2012).
82. Ventrella, D. et al. The p-ERG spatial acuity in the biomedical pig under physiological conditions. *Sci. Rep.* **12**, 1–9 (2022).

Acknowledgements

The Authors thank Dr. M.M. La Vail (Beckman Vision Center, University of California San Francisco, CA) for kindly providing non-dystrophic RCS-rdy$^+$ and dystrophic RCS rats; Prof. Guglielmo Lanzani (Istituto Italiano di Tecnologia, Milano, Italy) and Dr. Giovanni Manfredi (Novavido srl, Bologna, Itay) for useful discussions and advice in the preparation of nanoimplants; Dr. A. Russo (Department of Ophthalmology, Sacrocuore Don Calabria Hospital, Negrar, Italy) for assistance in the subretinal microinjections in rat and pig; R. Ciancio, I. Dallorto, A. Mehilli, R. Navone and D. Moruzzo (Istituto Italiano di Tecnologia, Genova, Italy) for technical assistance. The project has received funding from: the European Union's Horizon 2020 Research and Innovation Program under Grant Agreement No 881603 Graphene Flagship, Core3 WP5 "*Biomedical Technologies*"; the Istituto Italiano di Tecnologia Flagship program "*Technologies for Healthy Living*"; the Italian Ministry of Health (RF-2021-12374404) and the Italian Ministry of Foreign Affairs and International Cooperation (MAE00694702021-05-2); the Italian Ministry of University and Research (PRIN 2020WMSNBL); H2020-MSCA-ITN 2019 "*Entrain Vision*" (project 861423); #NEXTGENERATIONEU (NGEU) and funded by the Ministry of University and Research (MUR), National Recovery and Resilience Plan (NRRP), project MNESYS (PE0000006)–A Multiscale integrated approach to the study of the nervous system in health and disease (DN. 1553 11.10.2022); and IRCCS Ospedale Policlinico San Martino (Ricerca Corrente and 5x1000 grants).

Author contributions

F.G., J., and E.C. synthesized and characterized the nanoimplants. M.L.D. and J. performed the in vitro experiments in primary neurons. T.R., F.G., and E.C. performed and analyzed the ex vivo MEA experiments. G.P., M.A., S.F., F.G., G.M., and T.G. performed rat surgery. S.C., T.G., and F.G. performed and analyzed the retina histochemistry. S.F., M.L.D., S.C., T.G. and F.G. performed and analyzed the behavioral tests in the rat. S.D.M., S.C., T.G., S.D.M., and F.G. performed the PLR experiments. F.G. and S.F. performed the VEP measurements in the rat. J.F.M.V., S.D.M., D.V., M.L.B., G.P., E.C., A.E., and M.A. performed the experiments on the pig. F.B. and E.C. conceived the work, planned the experiments, analyzed the data, and wrote the manuscript. Grants to F.B. supported the project.

Competing interests

The authors declare no competing interests.

Additional information

Supplementary information The online version contains supplementary material available at https://doi.org/10.1038/s41467-025-63716-4.

Correspondence and requests for materials should be addressed to E. Colombo.

Peer review information *Nature Communications* thanks the anonymous reviewer(s) for their contribution to the peer review of this work. A peer review file is available.